ATMOSPHERIC ENVIRONMENT: X 29 (2026) 100417

Contents lists available at ScienceDirect

Atmospheric Environment: X

journal homepage: www.journals.elsevier.com/atmospheric-environment-x

# Improved methane flux estimation from hyper-spectral imagery via log-domain matched filtering and background homogenization[☆]

Fabrizio Masin, Tiziano Maestri[*], Michele Martinazzo, Giorgia Proietti Pelliccia

*Department of Physics and Astronomy 'Augusto Righi' - University of Bologna, viale Berti-Pichat, 6/2, Bologna, 40127, Italy*

## ARTICLE INFO

*Keywords:*
Methane
Background homogenization
PRISMA
Matched filter
Image spectroscopy

## ABSTRACT

New satellite hyper-spectral sensors, such as PRISMA of the Italian Space Agency, observe large portions of the Earth's surface at visible and at shortwave infrared wavelengths with high spectral and spatial resolutions, enabling the investigation of individual molecular species and the localization of emission sources. The 'Matched Filter' (MF) methodology, widely exploited in the methane source identification and in the estimation of enhanced concentrations, is discussed in its theoretical foundations, revised and extended within an integrated processing framework. We apply an estimator (termed MF-EVO) operating in the logarithmic radiance-ratio domain, i.e. optical depth space, which allows to overcome the limitations imposed by the linearization assumption of the classical MF and improves robustness across a wide range of methane concentration enhancements. Results from MF-EVO are compared to the traditional algorithm for a set of synthetic PRISMA observations accounting for both homogeneous and heterogeneous background conditions. The MF-EVO algorithm demonstrates superior performance over the MF-Classic method in identifying methane sources across all idealized conditions. Specifically, the estimated identification limit for $\Delta XCH_4$ is approximately 0.05 ppm for MF-EVO, significantly lower than the 0.09 ppm limit for MF-Classic. Furthermore, the MF-EVO consistently outperforms the classic MF in the accurate estimation of concentration enhancements across both small and medium-to-large methane concentration scenarios. Under idealized conditions, MF-EVO achieves an error margin within 5%, which is a substantial improvement compared to the 10%–50% error range observed with the MF-Classic method. To address the challenges posed by real-world scenes, the revised MF formulation is embedded in a processing chain that includes false-positive pixel elimination and scene homogenization through image partitioning into spectrally homogeneous clusters. These steps significantly reduce background-induced artifacts and stabilize methane enhancement retrievals, enabling more reliable plume identification and flux estimation. In the application to the Mumbai metropolitan landfills, the full processing chain reduces the estimated methane fluxes by approximately 40%–55% with respect to the classical MF applied to the full scene, highlighting the impact of background homogenization and false-positive suppression on flux estimation in heterogeneous environments.

## 1. Introduction

Methane ($CH_4$) is one of the dominant anthropogenic climate-forcing agents (GCP, 2023), accounting for about 35% of global anthropogenic emissions (Saunois et al., 2025). An increase in methane concentrations induces radiative forcing both directly and indirectly, by decreasing OH concentration in the atmosphere (Kurtén et al., 2011). Thus, the detection and reduction of unintended methane emissions from anthropogenic activities has been identified as a key means to decrease greenhouse gas concentrations in the atmosphere (United Nations Environment Programme, 2021).

Unlike carbon dioxide ($CO_2$), whose atmospheric variability is strongly affected by seasonal photosynthetic cycles, particularly in the boreal hemisphere, $CH_4$ presents a more intricate balance between natural and anthropogenic sources. Stable carbon isotope analyses have highlighted these differences: while $CO_2$ increases are primarily driven by fossil fuel combustion, partially compensated by photosynthetic uptake (Vieth and Wilkes, 2010; Graven et al., 2020), $CH_4$ trends have been shaped by shifts in dominant emission sources. In particular, recent studies suggest that natural sources, especially wetlands, are

---

[☆] Funding: This study was carried out within the Space It Up project funded by the Italian Space Agency, ASI, Italy, and the Ministry of University and Research, MUR, Italy, under contract n. 2024-5-E.0 - CUP n. I53D24000060005.

[*] Correspondence to: Dipartimento di Fisica e Astronomia 'Augusto Righi', via Irnerio 46, 40127, Bologna, Italy.
*E-mail address:* tiziano.maestri@unibo.it (T. Maestri).

https://doi.org/10.1016/j.aeaoa.2026.100417
Received 17 March 2025; Received in revised form 22 December 2025; Accepted 25 January 2026

currently major contributors to the observed global increase in atmospheric $CH_4$ (Nisbet et al., 2016; Michel et al., 2024). The anomalous rise in $CH_4$ concentrations during 2020 (despite the global reduction in human activities due to the COVID-19 pandemic) further underscores the complexity of $CH_4$ dynamics and the interplay between natural and anthropogenic processes (Laughner et al., 2021; Peng et al., 2022). Additionally, CH4 is a potent greenhouse gas with relatively short atmospheric lifetimes. Its global warming potential over 20 years (GWP20) is far greater than that of CO2, while its 100-year value (GWP100) remains approximately 28 times higher (Myhre et al., 2013; Sand et al., 2023; IPCC, 2023). These characteristics reinforce the need for comprehensive monitoring approaches capable of capturing both large-scale variability and localized emission events—including those beyond the reach of conventional in-situ atmospheric observation sites.

Spectrally resolved satellite radiances in the thermal infrared (with wavelengths ranging from about 4 to 16 μm) are used to derive methane column profiles (Smith et al., 2007). This type of inversion process is routinely applied to infrared sounders such as IASI (Clerbaux et al., 2009), CrIS (Han et al., 2013), and AIRS (Aumann et al., 2003), which are generally characterized by ground field-of-views of the order of 10 km. In recent years, spectrally resolved measurements of solar radiation reflected by the Earth's surface and atmosphere in the shortwave infrared (SWIR, 0.7–2.5 μm) have become available at very high spatial resolution (better than 50 m) and are increasingly used to retrieve methane and other trace gas concentrations from space. For the identification of methane emission sources and quantification of enhanced concentrations, the absorption occurring in the 2200–2300 nm band is generally used. However, retrievals from tropospheric monitoring instruments operating in the VIS–SWIR spectral range are inherently subject to well-known limitations: data coverage can be reduced by atmospheric or geographical conditions (e.g., cloud cover, complex terrain, or large water bodies), water vapor inhomogeneities and aerosol loading can affect retrieval accuracy, and the detection threshold for individual emissions remains higher than that of in-situ techniques. These factors can lead to discrepancies between satellite-based and surface-based estimates.

The flagship satellite mission for global methane monitoring is the TROPOspheric Monitoring Instrument (TROPOMI) onboard the Copernicus Sentinel-5 Precursor satellite (Veefkind et al., 2012). It provides accurate methane column concentration ($XCH_4$) data derived from a high spectral resolution ShortWave InfraRed (SWIR) channel and global daily coverage. However, its coarse spatial resolution (approximately $7 \times 7$ km$^2$, $7.0 \times 5.5$ km$^2$ since August 2019) limits the punctual identification of methane sources and restricts its use to the detection of widespread hotspots or locations with very intense emissions (Cusworth et al., 2018; Zhang et al., 2020; Pandey et al., 2019; Varon et al., 2019). Another relevant instrument for regional-scale methane monitoring is the JAXA-operated Global Observing SATellite for Greenhouse gases and Water cycle (GOSAT-GW) and its successors (Kuze et al., 2009; Suto et al., 2021). Several other satellite missions capable of mapping methane sources are currently in operation. A representative example is the GHGSat private constellation, designed specifically for methane retrieval and recognized as one of the most important players in high-resolution spaceborne mapping (Varon et al., 2019, 2020a). The GHGSat mission relies on a Fourier-transform spectrometer sampling the 1700 nm methane band at high spectral resolution (Jervis et al., 2021). However, limited data accessibility and low spatio-temporal coverage restrict its widespread scientific use. In parallel, imaging spectrometry (or hyperspectral imaging) has emerged as a promising technology for methane mapping. These instruments cover the solar spectrum from approximately 400 to 2500 nm, combining high spectral resolution (5–10 nm) with medium-to-high spatial resolution (around 30 m for satellite instruments). Although not optimized for methane detection, they sample the 2300 nm absorption feature with tens of channels, which can be exploited for identifying localized emission sources. The potential of spaceborne imaging spectrometers for methane mapping was first demonstrated using Hyperion data from the Aliso Canyon disaster (Thompson et al., 2016). Subsequent simulation-based studies (Cusworth et al., 2019; Ayasse et al., 2019) confirmed the feasibility of this approach, though progress was limited by the scarcity of suitable data. This situation changed with the launch of PRISMA (PRecursore IperSpettrale della Missione Applicativa – meaning "Hyperspectral Precursor of the Application Mission") by the Italian Space Agency (ASI) in 2019 (Cogliati et al., 2021). PRISMA provides open-access hyperspectral imagery with a spectral resolution of 10 nm and a spatial resolution of 30 m in the 400–2500 nm range. It represents a major step forward in operational hyperspectral observation from space. It is also worth mentioning that multispectral imagers such as Sentinel-2 and Landsat have been shown capable of detecting strong methane emissions in specific scenarios (Varon et al., 2020b), although their detection limits are higher than those of hyperspectral instruments due to coarser spectral sampling. In parallel to these satellite-based developments, continuous and highly precise measurements of greenhouse gases are performed by ground-based infrastructures. In Europe, the Integrated Carbon Observation System (ICOS) provides high-quality, standardized observations of $CH_4$ and other greenhouse gases at multiple sites, forming the fundamental reference for atmospheric monitoring and model validation. In Italy, the Mount Cimone Observatory, located in the northern Apennines and part of the ICOS network, has been conducting long-term $CH_4$ monitoring and regional variability studies (e.g., Fratticioli et al., 2023). More recently, the Italian atmospheric network has expanded to include stable carbon isotope measurements ($\delta^{13}C$–$CH_4$), providing valuable information on the methane source attribution and emission processes (Buono et al., 2025; Zazzeri et al., 2017).

At the international level, coordinated efforts are also underway to harmonize methane monitoring and reporting practices. The UNEP International Methane Emissions Observatory (IMEO) promotes transparent, science-based reporting of methane emissions and supports the integration of satellite and ground-based observations into global emission inventories (IMEO, 2025). Similarly, the CEOS Greenhouse Gas Task Team is developing Common Practices for Reporting Satellite-derived Facility-Scale Methane Emissions, establishing methodological guidelines to ensure consistency and comparability across missions and instruments (CEOS, 2025).

In this study, revised methodologies for satellite data analysis are applied to real-world cases, with the Bologna province serving as a representative example situated within this broader observational framework. The proposed hyperspectral retrieval approach aims to complement, rather than replace, existing surface-based infrastructures by extending their spatial representativeness and improving the detection of localized emission sources. This set the basis for future work to explore the validation of the MF-EVO methodology through direct comparison with ICOS and national observatory datasets, as well as with isotopic field surveys in urban environments.

The current leading satellite instruments in the monitoring of methane concentrations are characterized by a very high spectral resolution and a coarse spatial resolution (e.g. 0.25 nm in the SWIR and 7 km for TROPOMI). This allows a very accurate estimate of the column average of the mixing ratio of methane ($XCH_4$) in the region covered by the sensor, calculated as the ratio between the vertical column density of $CH_4$ and the vertical column density of dry air. By using high spatial resolution sensors, it is possible to aim for a different retrieval target variable: the per-pixel enhancement of the methane column concentration with respect to the background value ($\Delta XCH_4$). Two main approaches have been used for the retrieval of $\Delta XCH_4$ with imaging spectroscopy: physically-based and data-driven methods. Physically based methods rely on the modeling of the radiative transfer accounting for the radiation interaction with the surface and the atmospheric components. An example of this approach is the family of differential optical absorption spectroscopy (DOAS) methods, which have been used since AVIRIS and AVIRIS-NG airborne data (Thorpe et al., 2017;

Borchardt et al., 2020). Data-driven methods constrain the retrieval with information extracted from the image through statistical methods and are characterized by a superior computational efficiency with respect to the physically-based methods. Examples of methods based on the matched filter or the singular value decomposition concept successfully used with imaging spectroscopy data can be found in Thompson et al. (2016), Foote et al. (2020), Thorpe et al. (2014).

The goal of this article is to present an integrated processing chain for methane enhancement and flux estimation from hyperspectral imagery, centered on an evolved log-domain Matched Filter (here termed MF-EVO) (Thompson et al., 2016; Pei et al., 2023) and complemented by false-positive suppression and scene homogenization strategies. We argue that improvements in methane flux estimation from hyperspectral imagery cannot rely solely on refinements of the matched filter formulation. Instead, robust performance in heterogeneous real-world scenes requires an integrated processing chain, combining a physically consistent retrieval (like a log-domain MF) with explicit strategies for background homogenization and false-positive suppression. While the MF-EVO improves concentration enhancement estimates at the pixel level, the largest practical benefits emerge when it is embedded within this broader scene-level framework, particularly for extended emission sources.

Section 2 discusses the theoretical basis of the classical Matched Filter (MF) algorithm and introduces the improved algorithm, Matched Filter Evolution (MF-EVO).

The performance of both algorithms is tested in Section 3 under conditions of weak and strong methane emissions to assess their accuracy in source identification and flux quantification. This section also evaluates the ability of the filters to detect Gaussian-distributed enhancements and their sensitivity to baseline methane concentrations.

Section 4 analyzes images acquired by the PRISMA hyperspectral sensor for the detection of both punctual and spread methane emitters in urban and heterogeneous environments.

Section 5 examines homogenization strategies aimed at improving concentration estimates, which include false alarm elimination and background homogenization via scene partitioning. Issues related to methane detection in heterogeneous scenes, characterized by multiple surfaces reflectivity and variation in elevation, are accounted for and solutions for the scene homogenization are proposed.

The conclusions are drawn in Section 6.

## 2. Matched filter method for methane sources identification

The Matched Filter method is widely used in literature for its very promising results in the identification of $CH_4$ emissions with hyperspectral satellites. MF is applied efficiently in clear sky (with negligible aerosol load) and for wavelengths of about 2 μm. For these conditions, the spectral radiance, $I$, arriving at the satellite is accurately modeled by a simple equation accounting for atmospheric attenuation and surface reflection only:

$$I = \frac{1}{\pi} r(\mu_s, \mu_{obs}) F \exp^{-(\frac{\tau}{\mu_s})} \exp^{-(\frac{\tau}{\mu_{obs}})} = \frac{1}{\pi} r(\mu_s, \mu_{obs}) F \cdot T_s T_{obs} \tag{1}$$

Symmetry in the azimuth angles is assumed and the dependency on the wavelength is omitted for brevity. The bi-directional reflectivity of the surface of the area investigated by the sensor is indicated by $r$, $\tau$ is the vertical optical depth of the atmosphere, $F = F_{toa} \cdot \mu_s$ is the solar irradiance accounting for the incident solar zenith angle$\mu_s$, and $\mu_{obs}$ is the observational zenith angle. The transmissivities from the Sun to the surface and from the surface to the satellite are written using the symbols $T_s$ and $T_{obs}$ respectively, and their product provides the 2-way transmittance $T$. At wavelengths affected by $CH_4$ absorption, both these terms decrease with respect to the background values when a $CH_4$ plume is present. In clear sky conditions (which are in the absence of clouds and minor aerosol concentration) and for small variations of water vapor concentration in the image, the radiance associated to the pixels observed by the hyperspectral imager depends on both the amount of methane along the Sun–Earth–satellite path and the surface properties. Thus, expanding Eq. (1) in terms of methane concentration and surface reflectivity, the radiance at the satellite is:

$$I \cong I(r_0, \rho_0) + \frac{\partial I}{\partial r} \Delta r + \frac{\partial I}{\partial \rho} \Delta \rho = r_0 I_0 T_0 + I_0 \Delta r T_0 + r_0 I_0 \frac{dT}{d\rho} \Delta \rho \tag{2}$$

where the term $r_0 I_0 T_0$ is used to indicate the mean radiance observed by the satellite, corresponding to the background (mean conditions of the observed scene) for the mean surface reflectance $r_0$ and the methane concentration $\rho_0$ which provides a two-way transmittance $T_0$. The incident radiance $I_0$ is obtained from $F_0/\pi$. The last two terms in the equation refer to radiance variation due to changes in the surface reflectivity ($\Delta r$) and $CH_4$ concentration ($\Delta \rho$) with respect to mean conditions.

For pixels whose surface reflectivity is larger than the mean conditions, the radiance arriving at the satellite is larger than the background value (due to a positive $\Delta r$) and smaller otherwise. An increase in methane concentration ($\Delta \rho > 0$), as a result of an emission plume, implies a negative variation in the two-way transmissivity and makes the last term of Eq. (2) negative. The result is that a variation in the surface properties (i.e. pixels with reflectivity smaller than the one representing the mean condition) can produce the same effect on the observed radiance as an increase in methane concentration. This is the reason why heterogeneous surfaces are extremely challenging for the identification of methane plumes and the matched filter method provides plenty of false alarms.

### 2.1. Matched filter classical algorithm

The use of the Matched Filter (MF) method for methane source identification is very popular for many reasons, among which its property to implicitly account for radiometric and spectral errors and, differently from physics-based methods, the capability to directly provide $\Delta XCH_4$ with respect to the mean conditions in the image, which facilitates the identification of possible emission sources. The MF method is based on the idea that each input spectrum can be expressed as the perturbation of an average radiance spectrum due to a change in the methane column concentration. The classical formulation of the MF (MF-Classic from now on), similarly to what was reported in Guanter et al. (2021), is:

$$\Delta XCH_4(\boldsymbol{I_p}) = \frac{(\boldsymbol{I_p} - \boldsymbol{I_c})^T \Sigma^{-1} \boldsymbol{t}}{\boldsymbol{t}^T \Sigma^{-1} \boldsymbol{t}} \tag{3}$$

$$\boldsymbol{t} = \boldsymbol{I} \cdot \boldsymbol{k} \quad [\frac{\mathrm{rad}}{\mathrm{ppm}}] \tag{4}$$

where $\mathbf{I}_p$ is the radiance spectrum of the pixel under analysis, $\mathbf{I}_c$ and $\Sigma$ are the mean radiance and the associated covariance matrix of the background. An explicit derivation of this filter is provided in Appendix A. The term $\mathbf{t}$ indicates the so-called target spectrum which is generated by the two terms $\mathbf{I}$, the mean value of the background radiance, and $\mathbf{k}$, with $k = dT/d\rho$ being the variation of the two-way vertical transmissivity due to an increase of 1 ppm of methane in an air column of 1 km (which is assumed a small increase).

Note that the variables $\mathbf{I}_c$ and $\Sigma$ are calculated on a per-column basis in order to account for the different radiometric responses of the detector elements across-track and, eventually, mitigate sensor's non-Gaussian artifacts. The target spectrum $\mathbf{t}$ is generated once for the whole image at a high spectral resolution, but the subsequent spectral convolution with the instrument's spectral response function is performed per-column to account for potential across-track variations of the instrument spectral response. The spectral window selected for the matched-filter methane retrieval may vary in accordance with the sensor characteristics and the algorithm used. However, the $CH_4$ absorption peak at 2300 nm is usually targeted.

### 2.2. *Matched filter EVO algorithm*

In this sub-section we describe a different approach to the MF methodology. First, we can consider a plane parallel atmosphere approximation and split the atmosphere into $n$ thin layers. The layer discretization of Eq. (1) is given by:

$$I = \frac{1}{\pi} r(\mu_s, \mu_{obs}) F \prod_{i=1}^{n} T^i(\mu_s) \prod_{i=1}^{n} T^i(\mu_{obs}) \tag{5}$$

where the superscript $i$ indicates the layer and the product is performed on the entire atmosphere from layer 1 to n. If a plume of absorbing gas is occupying a specific layer of the atmosphere, the equation describing the radiance at the observer can be written as:

$$I_p = \frac{r(\mu_s, \mu_{obs})}{\pi} F \prod_{i=1}^{n} T^i(\mu_s) T_p(\mu_s) \prod_{i=1}^{n} T^i(\mu_{obs}) T_p(\mu_{obs}) \tag{6}$$

Where $T_p$ indicates the contribution of the plume to the total transmissivity of the atmosphere. Specifically, we have:

$$T_p(\mu) = e^{(-\frac{\sigma_p \rho_p \Delta z}{\mu})} \tag{7}$$

With $\Delta z$ the geometrical thickness of the layer containing the plume, $\sigma_p$ is the absorbing cross-section of the plume gas and $\rho_p$ is the additional gas concentration in the layer due to the plume. To obtain information about the latter from a radiometric measurement of $I_p$, we can write:

$$I_p = \frac{1}{\pi} r(\mu_s, \mu_{obs}) F \prod_{i=1}^{n} T^i(\mu_s) \prod_{i=1}^{n} T^i(\mu_{obs}) e^{-\Delta z \sigma_p \rho_p (\frac{\mu_s + \mu_{obs}}{\mu_s \mu_{obs}})} = I e^{-\Delta z \sigma_p \rho_p (\frac{\mu_s + \mu_{obs}}{\mu_s \mu_{obs}})} \tag{8}$$

Defining $k$ as the rate of change of the two-way transmissivity due to the plume in the layer with geometrical thickness $\Delta z$ brings to:

$$k = \frac{\partial}{\partial \rho_p} e^{-\Delta z \sigma_p \rho_p (\frac{\mu_s + \mu_{obs}}{\mu_s \mu_{obs}})} |_{\rho_p = 0} = -\Delta z \sigma_p (\frac{\mu_s + \mu_{obs}}{\mu_s \mu_{obs}}) \tag{9}$$

Eq. (9) defines the meaning of $k$ which is the optical depth for a gas unit concentration increase from a zero starting point. Its formulation is derived without relying on any approximation for weak absorption as in the classical algorithm since no assumptions on layer transmissivity are considered. The observed radiance in presence of the plume is then written as:

$$I_p = I e^{k \rho_p} \tag{10}$$

From which it is possible to derive the enhanced methane concentration ($\Delta XCH_4$) as:

$$\rho_p = \ln(\frac{I_p}{I}) \frac{1}{k} \tag{11}$$

To derive an optimal filter for this quantity, we can assume a description of the observed radiance as:

$$I_p \propto I \cdot \epsilon \tag{12}$$

With $\epsilon$ a multiplicative error. The choice of using a multiplicative error is justified by the fact that many natural phenomena produce log-normally distributed errors, where observations result from multiplicative combinations of independent factors. The derivation of the filter follows from here the same steps of the classical filter derivation, as shown in Appendix A, starting from the definition of $x$ as:

$$x = ln\left(\frac{I_p}{I(r_0, \rho_0)}\right) = k \cdot \rho_p + ln(\epsilon) = k \cdot \rho_p + \epsilon' \tag{13}$$

The final form for the matched filter will be:

$$\Delta XCH_4(\boldsymbol{I}_p) = \rho_p = \frac{\ln(\frac{I_p}{I})^T \Sigma^{-1} \boldsymbol{k}}{\boldsymbol{k}^T \Sigma^{-1} \boldsymbol{k}} \tag{14}$$

In our case $\boldsymbol{I}_p$ and $\boldsymbol{I}$ are the vectors containing the measured radiances at different wavelengths (or channels) for the plume observation and for the average scenario (no plume) respectively. The last term is obtained by using a geometric mean over the radiance coming from the image pixels. $\Sigma$ is the covariance matrix of the quantity $\ln(\frac{I_p}{I})$ for the different observational channels, and $\boldsymbol{k}$ is the vector containing the rate of change of the two-way transmissivity at the different wavelengths. It is important to note that the discretization allows for a more correct description of the coefficient $\boldsymbol{k}$. Specifically, the value of $\boldsymbol{k}$ can be computed by considering the contribution of each layer to the total optical depth change, due to methane concentration's variations.

An equivalent formulation of the MF is obtained in Schaum (2021) and subsequently in Pei et al. (2023), although derived from considerations on the statistical distribution of the observed background radiance instead of general physical principles. Together, both the physical rationale and the statistical arguments provide strong theoretical foundations for this revised formalization of the matched filter. While MF-EVO significantly improves the stability and physical consistency of methane enhancement retrievals, its optimal performance still relies on the validity of the homogeneous-background assumption. In real scenes, this assumption is often violated, motivating the scene-level preprocessing and homogenization strategies introduced in Section 5.

### 2.3. *Methane flux estimation*

To compare the results obtained in our analysis with similar cases in the literature, we use the Integrated Methane Enhancement (IME) model already tested in Guanter et al. (2021), Frankenberg et al. (2016) and Varon et al. (2018) for the plume flux estimation. The methodology requires that a polygon is manually defined for each plume, to isolate the plume pixels from the background. The emission flux rate (Q), in kg/h, derives from the estimation of the IME in unit of kg as the total excess mass of methane contained in the plume:

$$IME = k_{CH_4} \sum_{i=1}^{n_p} \Delta XCH_4(i) s_i \tag{15}$$

where $s_i$ is the surface area of the pixel, $k_{CH_4}$ is a scaling factor converting the total pixel-wise methane concentration values to kg by assuming Avogadro's Law and taking into account molecular weight of methane, and the summation is on $n_p$, the total number of pixels in the plume. In our calculations:

$$k_{CH_4} = 16.043[\frac{g}{mol}] \cdot \frac{1}{0.022}[\frac{mol}{m^3}] \cdot \frac{1}{10^6}[ppm^{-1}] = 0.716 \cdot 10^{-6}[\frac{g}{ppmm^3}] \tag{16}$$

as derived in Foote et al. (2021). Q is then computed as:

$$Q = \frac{U_{eff} \cdot IME}{L} \tag{17}$$

where $U_{eff}$ is an effective wind speed and $L$ is the plume length scale factor (square-root of the plume mask area). The $U_{eff}$ term is obtained from the 10-m wind speed, $U_{10}$, by using the following relation:

$$U_{eff} = 0.34 \cdot U_{10} + 0.44 \tag{18}$$

Eq. (18) is derived using the same methodology described in Varon et al. (2018) and the $U_{10}$ data can be derived from ERA5 (ERA5, 2025). Fluxes of real case scenarios are discussed in Sections 4.1 and 4.2, and presented with error ranges. The range is established by the propagated error on the main components of the flux calculation just described: the uncertainty on wind speed and direction (the most influential factor) and the error associated with the IME estimation itself. A marginal contribution from possible plume segmentation uncertainty is also considered. The total estimated error amounts to approximately 70% (Foote et al., 2021; Cusworth et al., 2021).

## 3. Assessment of $CH_4$ concentration enhancement detection and quantification for idealized conditions

Currently, a clear assessment of the detection threshold of the MF method is still lacking. Some attempts are described in Guanter et al. (2021) where simulated plumes of various flux sizes are successively

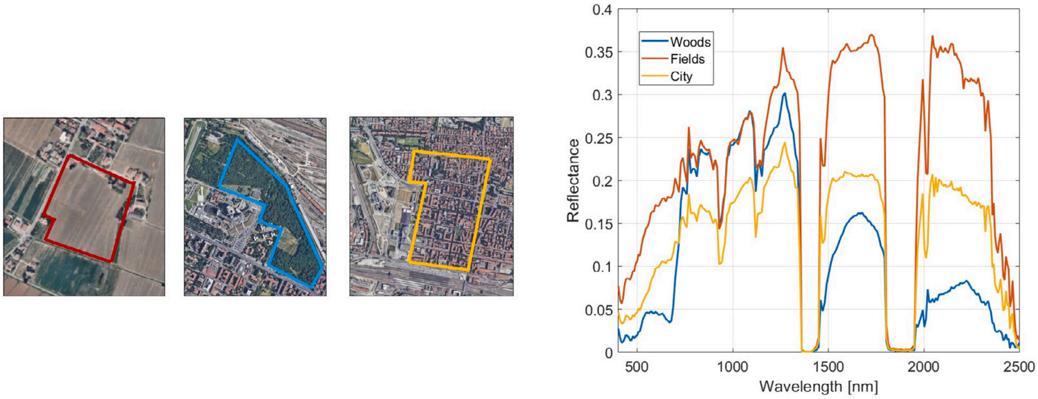

**Fig. 1.** *Background Spectral Reflectivities* - Left: Google Earth views of the areas used as reference for the spectral reflectivities: fields in Santa Viola (red), the urban woods "Prati di Caprara" (blue) and the Bolognina neighborhood (gold). Right: Spectral reflectivities assumed for the three considered backgrounds (see legend). Spectral values over the PRISMA range are obtained from spatial averages. (For interpretation of the references to color in this figure legend, the reader is referred to the web version of this article.)

superimposed on observed scenes. In this section, elementary synthetic scenarios are generated to evaluate the MF ability to detect $CH_4$ enhancements and estimate their amount with respect to the background conditions. We consider both MF-Classic and MF-Evo applied to a satellite hyper-spectral imager such as Italian Space Agency (ASI) sensor PRISMA (Cogliati et al., 2021). This means that the PRISMA spectral resolution, noise level and instrumental response function are considered in the simulations.

The analyses presented in this section are intentionally performed on idealized conditions and thus without applying false-positive elimination or scene partitioning. This choice allows us to isolate the intrinsic behavior of the MF-EVO formulation relative to the classical MF under controlled conditions. In real world applications, however, the performance gains discussed here represent only part of the overall improvement, as additional benefits arise from the full processing chain described in Section 5.

The line by line LblRTM code (lblRTM, 2023) is run for the calculation of the high-spectral resolution gas absorption optical depths. In all the simulations, the absorption features of the atmosphere are calculated considering the climatological concentrations of six molecular species, the most absorbing ones at SWIR wavelengths: water vapor, carbon dioxide, ozone, nitrous oxide, carbon monoxide and methane. An in-house code, derived from the algorithm described in Korkin et al. (2022), which solves the radiative transfer equation at high-spectral resolution accounting for a bi-directional reflectivity and, possibly, Rayleigh scattering, is used.

For simulations of the radiance spectra, we rely on reflectance values obtained from a real PRISMA image. The reference observation refers to an image that contains the Metropolitan Area of Bologna, taken in November 2020 (Agenzia Spaziale Italiana (ASI), 2025). The spectral reflectivities used in the simulations are obtained by averaging, on each PRISMA channel, the reflectivity measured by PRISMA on three different homogeneous areas identified on the image as shown in Fig. 1. In all the tests performed, three different backgrounds, in terms of reflectivity, are considered. The selected areas, representative of commonly found reflective conditions, are:

- a densely vegetated area (*woods*): Prati di Caprara urban forest - $44^{\circ}30'30''N\ 11^{\circ}18'55''E$
- a strongly anthropized area (*city*): the Bolognina neighborhood - $44^{\circ}30'41''N\ 11^{\circ}20'45''E$
- a cultivated area (*fields*): fields near Santa Viola (province of Bologna) - $44^{\circ}36'23''N\ 11^{\circ}15'12''E$

The PRISMA image, used to derive the reference surface reflectivities, is used to define the Instrument Viewing Angle and the Solar Zenith Angle which are extracted from the associated metadata. Once the high-spectral resolution simulations are computed, a convolution with the PRISMA Instrumental Response Function (IRF) is performed. The IRF is assumed Gaussian, centered in the nominal wavelength of each sensor channel and with an associated standard deviation $\sigma = FWHM/2.355$. The central wavelength and the Full Width at Half Maximum (FWHM) of each channel are available from PRISMA metadata. Noise equivalent spectral radiance is added to the synthetic PRISMA observations as a randomly generated value obtained from a normal distribution with zero mean and standard deviation such that $3\sigma = 0.01 \cdot I_{px}$ where $I_{px}$ is the radiance value of each pixel in the scene. This choice is made in accordance with the definition of the PRISMA noise level which, in the spectral region of interest, is derived from the specification that the signal to noise ratio $SNR \geq 100$ at 2300 nm (Agenzia Spaziale Italiana (ASI), 2020).

The simulation tests consist of study cases characterized by simplified background conditions. Typically we assume that the surface reflectivity of the background is taken by one or two types of reflectivities proposed above, and the atmospheric conditions are the same as in the image. In each case study, three 'patches' are considered. A patch is defined as a group of pixels (25 in our simulations) with methane concentration different from those assumed for all the other pixels. The patches are placed in the top-left, at the center and in the bottom-right part of the images.

### 3.1. Small methane concentration enhancements

The first idealized case study consists of a PRISMA-like observation of a homogeneous background in terms of surface reflectivity and atmospheric gas concentrations. We assume that the homogeneous scene is distinguished by three patches, each comprising 5 by 5 pixels in the image, which are characterized by an enhancement in the concentration of $CH_4$ with respect to the background atmospheric conditions. We assume that, with respect to the background methane concentration, the $\Delta XCH_4$ are:

- Top-left patch: 1 ppm
- Center patch: 0.5 ppm
- Bottom-right patch: 0.1 ppm

The PRISMA-like observed radiances of the three patches are calculated in the same way as the radiance computed for the background, but using optical depths adjusted for the increase in concentration of $CH_4$ in the last kilometer of air column. The concentration profiles of the other molecules are left unchanged. All the simulations account for the PRISMA sensor noise.

**Table 1**
Estimates of the $CH_4$ enhancements illustrated in Fig. 2 for three different surface background (BG) conditions representatives of woods, rural fields and city. The reported values are the averages on each single patch obtained using the classical MF or the EVO algorithm.

| *Reference enhancements* [ppm] | *1* | *0.5* | *0.1* |
|---|---|---|---|
| **MF Classic** | | | |
| BG woods | 1.11 | 0.55 | 0.11 |
| BG field | 1.12 | 0.56 | 0.11 |
| BG city | 1.12 | 0.57 | 0.10 |
| **MF EVO** | | | |
| BG woods | 1.05 | 0.52 | 0.11 |
| BG fields | 1.05 | 0.53 | 0.10 |
| BG city | 1.05 | 0.53 | 0.10 |

**Table 2**
Estimated $\Delta XCH_4$ for the scenarios depicted in Fig. 3 accounting for an image characterized by two surface reflectivities. The reported values are the average enhancement of each patch.

| *Reference enhancements* [ppm] | *1* | *0.5* | *0.1* |
|---|---|---|---|
| Woods/field - Classic | 0.72 | 0.36 | 0.15 |
| Woods/field - EVO | 1.03 | 0.51 | 0.10 |
| Field/woods - Classic | 1.53 | 0.78 | 0.07 |
| Field/woods - EVO | 1.04 | 0.52 | 0.11 |

The application of MF-Classic and MF-EVO to idealized conditions accounting for a homogeneous background including the three patches of 1, 0.5 and 0.1 ppm of methane provides the results of the $\Delta XCH_4$ summarized in Table 1. The corresponding $\Delta XCH_4$ maps and pixel distributions are depicted in Fig. 2.

Results presented in Table 1 demonstrate that both methodologies are effective in identifying the area affected by a methane concentration enhancement, even for the weakest case considered ($\Delta XCH_4$ = 0.1 ppm), and independently of the assumed surface background. Fig. 2 illustrates the effect of the measurements' noise on estimated $\Delta XCH_4$ values for the two MF methods utilized. Specifically, the $\Delta XCH_4$ values derived from background pixels using MF-EVO exhibit less spread around the zero mean than those obtained using MF-Classic. This reduced variability significantly facilitates the identification of true methane enhancements when employing MF-EVO, despite the comparable enhancement values estimated by the two methods. This is visually shown in Fig. 2 for the patch with $\Delta XCH_4$=0.1 ppm and the observation holds true for all three investigated cases. Assuming a detection limit corresponding to the 98% percentile of the background pixel distributions, we compute the identification limit to $\Delta XCH_4$ values of about 0.047 ppm for the MF-EVO and 0.085 ppm for the MF-Classic.

To evaluate the effect of surface reflectance heterogeneity on the identification of methane sources and on the derivation of the concentration enhancement, two different types of backgrounds for the same image are assumed. We consider that a first type of surface occupies the upper part of the image and a second type the lower one. As in the previous case study, the patches are placed at the top-left, in the center and at the bottom-right part of the image. For this case study the patches in the top left and at the center are characterized by pixels of the first type of background, while the bottom-right patch pertains to the family of the second type of reflectance.

The simulation results are shown in Fig. 3 for the combination of reflectivities representative of woods and fields. The Figure illustrates the radiance map at 2300 nm (left column) and the resulting $\Delta XCH_4$ after applying the MF-Classic (center column) and the MF-EVO (right column). The two columns of the Figure differ in the collocation of the type of surface: woods in the top half of the image and cultivated fields in the bottom half in the right column and vice-versa in the left one. The Figure shows that the MF-EVO is less sensitive to surface inhomogeneities than the MF-Classic. It is observed that the $\Delta XCH_4$ values obtained using MF-EVO, referring to background pixels, are more homogeneous than those obtained using MF-Classic. We note that, when using MF-Classic, the $\Delta XCH_4$ values of the BG pixels are correlated with the type of surface reflectance considered, as can be seen in the center column of Fig. 3. This effect also affects the estimation, by using the MF-Classic, of the methane concentration increase in the patches as can be seen from the numerical values reported in Table 2. It is observed that, the concentration enhancement value is slightly underestimated when the patch lies in the area affected by the lower-radiance surface, and slightly overestimated elsewhere. By contrast, the MF-EVO method provides better estimates of $\Delta XCH_4$ for the two patches considered, and the concentration enhancement estimates are less dependent on the assumed background reflectance values. Similar results (not reported) are found when different combinations of the three reference surfaces are assumed (woods/city and field/city).

**Table 3**
Results (in ppm) of the application of the MF-Classic method and of the MF-EVO for large methane enhancement concentration estimation above three different surface backgrounds (BG): woods, cultivated fields and city.

| *Reference enhancements* [ppm] | *5* | *10* | *20* |
|---|---|---|---|
| BG woods - Classic | 5.01 | 9.29 | 16.0 |
| BG woods - EVO | 4.76 | 9.56 | 19.1 |
| BG fields - Classic | 4.97 | 9.16 | 15.5 |
| BG fields - EVO | 4.78 | 9.57 | 19.2 |
| BG city - Classic | 4.98 | 9.10 | 15.4 |
| BG city - EVO | 4.78 | 9.55 | 19.2 |

### 3.2. *Large methane concentration enhancements*

In this Section we compare the ability of the MF-EVO algorithm with that of the MF-Classic to estimate the methane concentration enhancements in the presence of large concentration increases. The concentration enhancements considered in these idealized cases represent medium-to-strong signals, placing them well above the detection threshold for typical high-resolution remote sensing instruments. A simulation setup is arranged in a similar way to what is presented in Section 3.1. For this case, the $CH_4$ concentration enhancements associated with the three patches are significantly increased to simulate stronger emission sources.

The new concentrations enhancements are:

- top-left patch: 5 ppm
- center patch: 10 ppm
- bottom-right patch: 20 ppm

Note that the three values are selected because they are sufficient to demonstrate the different trends between the two formalizations, while still be representative of practical cases. In fact, a concentration enhancement of 10 ppm over an air column of 1 km would result, using the IME model described in Eq. (15), in a flux of 900 kg/h for a 10 m wind speed of 3 m/s. The above quantities are of the same order of magnitude as those discussed in the examples in Section 4.2. Furthermore, numerous studies in the literature report concentration enhancements exceeding 20 ppm, resulting from both anthropogenic and natural sources (Omidi et al., 2025; Etiope et al., 2019; Zazzeri et al., 2015, 2016).

Table 3 summarizes the numerical results of the simulations. Results show that the estimation accuracy of MF-Classic decreases with the increase of the methane concentration enhancements. MF-Classic performs with great accuracy for the 5 ppm case. For the largest enhancement considered (20 ppm) the discrepancies with respect to the true values reach 20%. The accuracy of the MF-EVO algorithm does not show any dependency on the absolute value of the methane concentration enhancement and the method performs within a 2% error

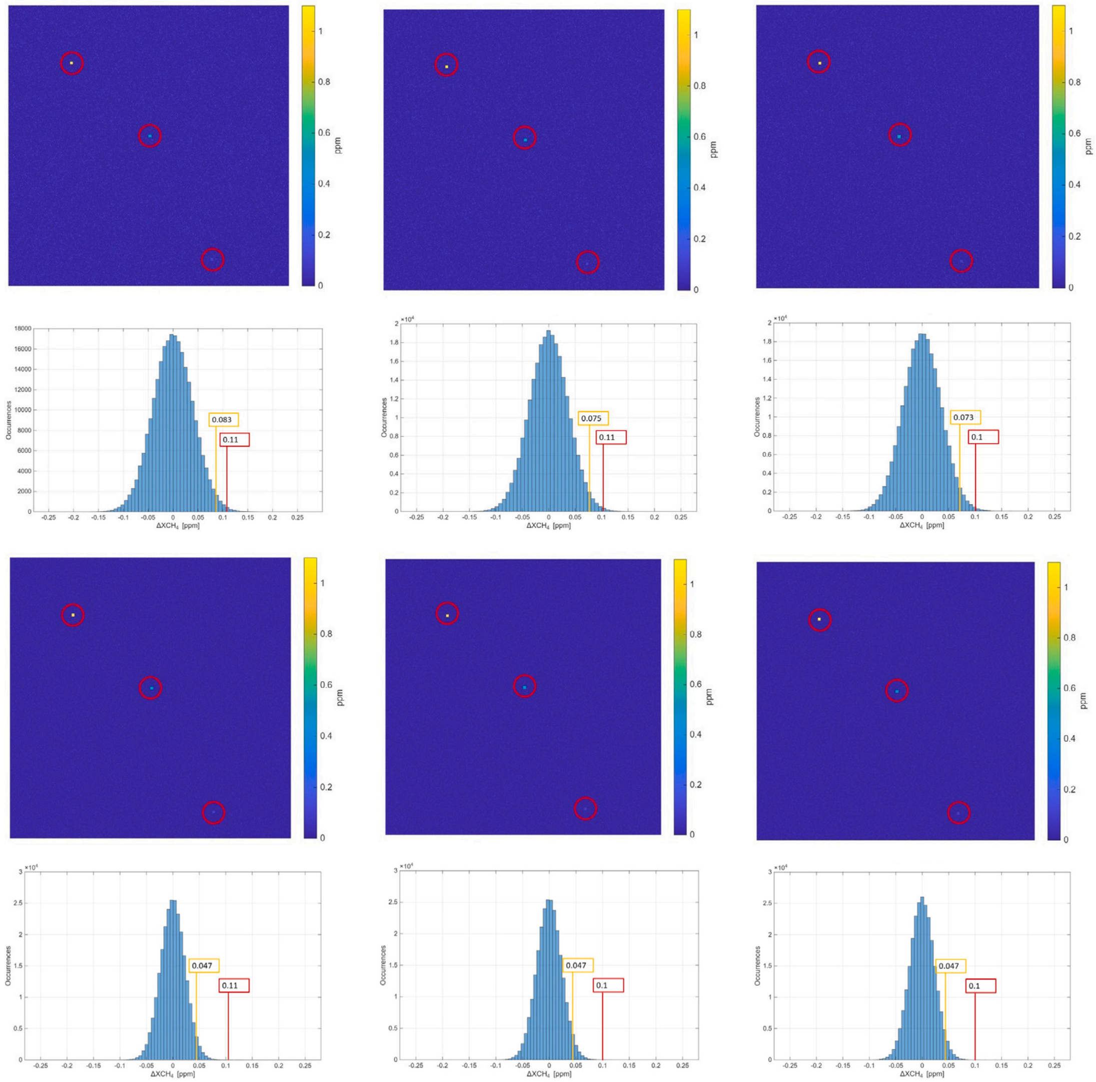

**Fig. 2.** *Simulation test on single background* - $\Delta XCH_4$ maps and corresponding pixel distributions for three ideal cases. MF-Classic is used for results shown in the top two rows and MF-EVO for the bottom two rows. Three different background reflectances are assumed representative of woods (left), cultivated field (center) and city (right). In the plots representing the $\Delta XCH_4$ histograms, the position of the average value of the bottom-right patch (enhancement of 0.1 ppm) is highlighted in red, while the value corresponding to a CDF of 98% is highlighted in orange. (For interpretation of the references to color in this figure legend, the reader is referred to the web version of this article.)

for all three patches considered. For both methods, we do not find any strong dependency on the assumed background.

### 3.3. Gaussian distributed enhancements

In the previous sections, uniform concentration patches were used to facilitate a quantitative evaluation of concentration enhancement estimates provided by the algorithms. However, it could be of interest to evaluate the performance of the two MFs in case of a distributed enhancement, such as the Gaussian distribution.

To obtain the desired Gaussian behavior on the patches of the simulated radiance maps, the transmittance associated with each pixel of the patch is multiplied by the factor $e^{2\Delta\tau(1-\chi)}$ where $\Delta\tau$ represents the optical depth difference between the background and the concentration enhancement in the patch and $\chi$ is a value of the 2-D Gaussian distribution applied to the given pixel. The Gaussian distribution is normalized to its maximum value so that $\chi$=1 at the central pixel.

The pixel-wise operation of the two algorithms demonstrates strong robustness to boundary fuzziness as shown in Fig. 4. The estimate at the central pixel (the only one actually exhibiting the nominal concentration enhancement) is consistent with the average values obtained for uniform patches, while the estimates over the surrounding pixels follow the expected trend of the adopted Gaussian mask. This behavior is confirmed for both the EVO and the Classic formalizations and for every BG considered.

### 3.4. Sensitivity to different baseline $CH_4$ concentrations

Given that the background value of the methane concentration varies with season and location (Agusti-Panareda et al., 2017), and that a global increasing trend has been observed over recent decades, it is worth assessing whether the estimation performance of the MF algorithms depends on the assumed baseline methane concentration. All the MF implementations presented in this study assume a baseline value of 1.86 ppmv, representative of background atmospheric methane

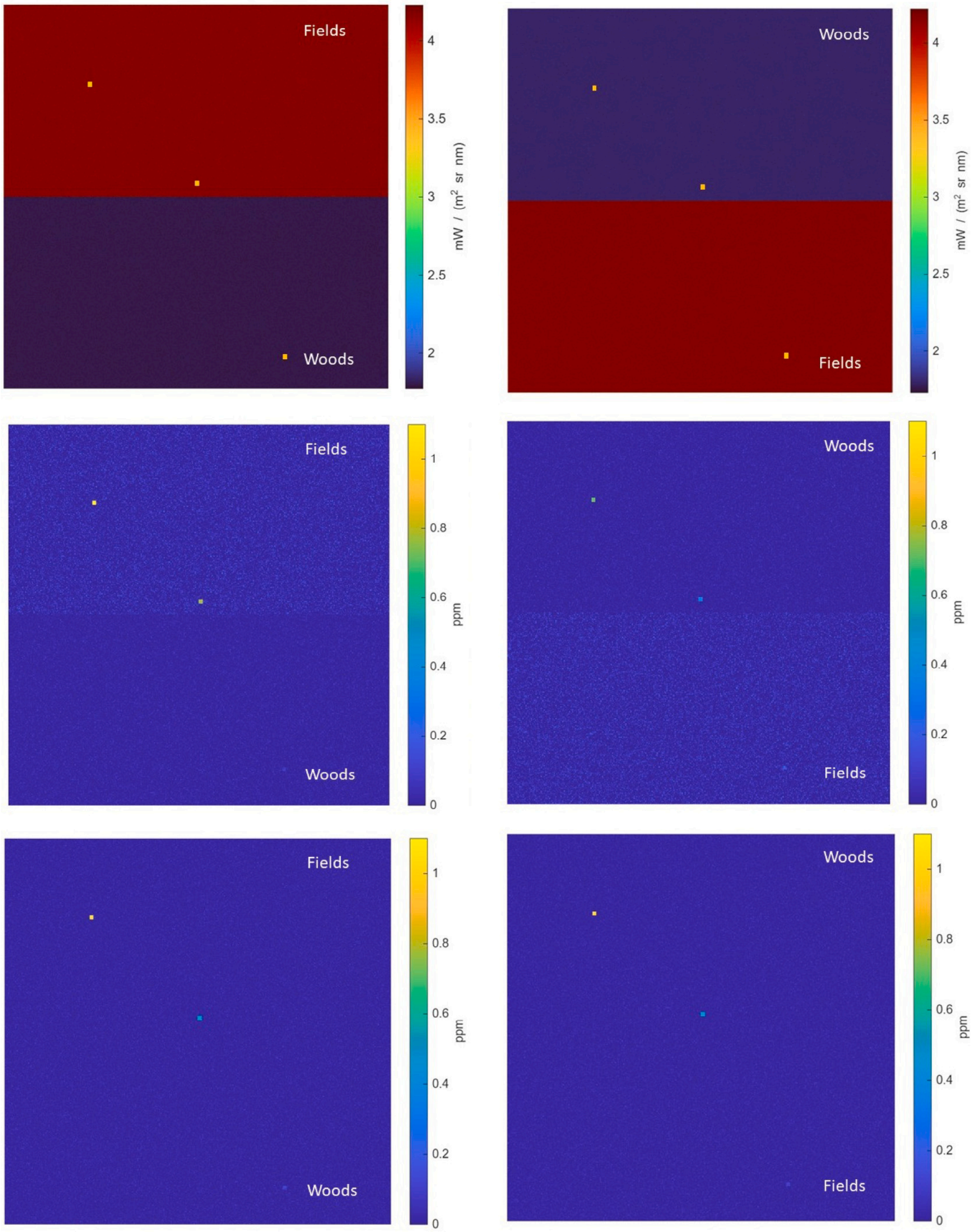

**Fig. 3.** *Simulation test on composite background* - Top row: PRISMA simulated radiances at 2300 nm for images considering two background reflectivities. Patches locations are highlighted as yellow box in the two upper panels. Center row: $\Delta XCH_4$ obtained applying the MF-Classic. Bottom row: $\Delta XCH_4$ obtained applying the MF-EVO. (For interpretation of the references to color in this figure legend, the reader is referred to the web version of this article.)

concentrations prior to the rapid increase observed over the past few years, and therefore below current global mean levels. The same simulations were thus repeated using baseline values of 2.2 ppmv and 2.6 ppmv. The corresponding results are reported in Tables 4 and 5.

The Tables show that the estimates remain highly consistent for both formalizations and for both weak and strong enhancement scenarios. This demonstrates that the method's performance is independent of the chosen baseline methane concentration. Consequently, we presented only the results obtained with a baseline of 1.86 ppmv in the main paper, acknowledging that conclusions are valid for any baseline value within the tested range.

## 4. Application of MF-EVO to PRISMA data

In the following applications, MF-EVO is first applied to PRISMA observations in its basic form to facilitate comparison with previous MF-based studies; the impact of false-positive suppression and scene homogenization on these same cases is analyzed separately in Section 5. We first apply the method to a literature case study to evaluate the consistency of the log-domain algorithm with previous results obtained using the MF-Classic. Successively, the MF-EVO is applied to PRISMA observations of widespread emission sources to prove the process of

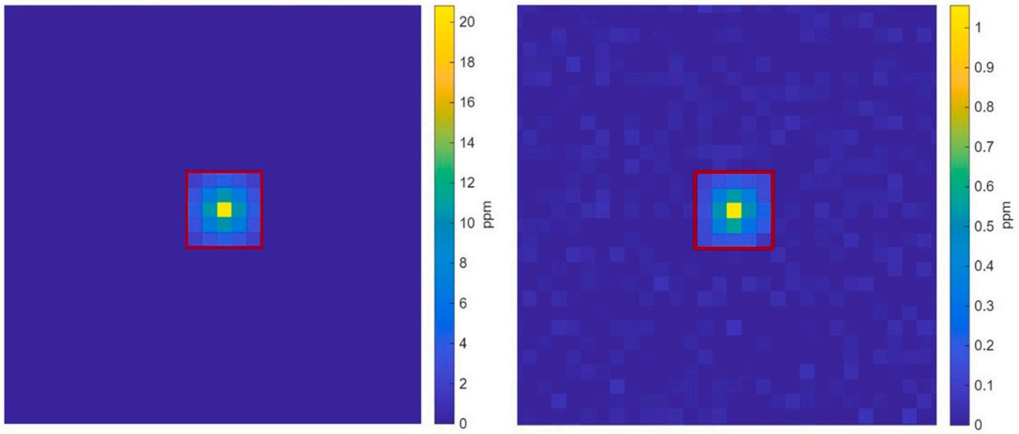

**Fig. 4.** *Gaussian distributed enhancement analysis* - Zooms on the $\Delta XCH_4$ values of the patches enhanced with 20 ppm (Left panel) and 1 ppm (Right panel). The MF-EVO is applied to an idealized uniform background with typical reflectivity of a city. The boundaries of the patches are highlighted in red. (For interpretation of the references to color in this figure legend, the reader is referred to the web version of this article.)

**Table 4**
Estimates of the $CH_4$ enhancements considering three different values as methane baseline concentration. MF Classic case.

| MF Classic - different baseline values | | | |
|---|---|---|---|
| | *1.86* ppmv | *2.2* ppmv | *2.6* ppmv |
| *0.1* ppm | 0.10 | 0.12 | 0.11 |
| *0.5* ppm | 0.57 | 0.55 | 0.57 |
| *1* ppm | 1.12 | 1.12 | 1.11 |
| *5* ppm | 4.98 | 4.95 | 4.98 |
| *10* ppm | 9.10 | 9.11 | 9.13 |
| *20* ppm | 15.38 | 15.41 | 15.50 |

**Table 5**
Estimates of the $CH_4$ enhancements considering three different values as methane baseline concentration. MF EVO case.

| MF EVO - different baseline values | | | |
|---|---|---|---|
| | *1.86* ppmv | *2.2* ppmv | *2.6* ppmv |
| *0.1* ppm | 0.10 | 0.11 | 0.11 |
| *0.5* ppm | 0.53 | 0.52 | 0.53 |
| *1* ppm | 1.05 | 1.05 | 1.05 |
| *5* ppm | 4.80 | 4.79 | 4.81 |
| *10* ppm | 9.55 | 9.55 | 9.58 |
| *20* ppm | 19.16 | 19.13 | 19.20 |

source identification and concentration enhancement estimation also for these conditions.

### 4.1. Punctual emission sources

The first implementation of MF-EVO for the derivation of $\Delta XCH_4$ maps aims at the detection of strong punctual sources, such as pipeline leakages in oil fields or strong emissions from coal mines. To this purpose, we start our analysis from previously studied data (Guanter et al., 2021). In particular, in Fig. 5 the results concerning coal mines and coal power plants in the Shanxi region (Agenzia Spaziale Italiana (ASI), 2025), China, are shown. The interest in this case study also lies in the fact that coal mines and associated infrastructure are recognized as a non-negligible component of the global methane budget. Throughout the life cycle of coal, emissions are released from both mining operations (particularly through ventilation and Coal Bed Methane recovery systems) and, indirectly, from the storage and handling of coal destined for thermal power plants (Zazzeri et al., 2016).

In the right panel of Fig. 5, the three plumes are perfectly visible along with other signals corresponding to roads and industrial buildings. These high signals arising from surface features, rather than actual methane enhancements, are discussed in Section 5. As a mean of both data verification and benchmarking, also the MF Classic algorithm is applied: the averaged concentration enhancements found for the three plumes are 0.94 ppm, 1.09 ppm and 0.93 ppm (from left to right). The flux estimation, following the steps described in Section 2.3, results in $3820 \pm 1540$ kg/h, $4075 \pm 1640$ kg/h and $3090 \pm 1250$ kg/h. These values are lower than the results found in Guanter et al. (2021) although they are of the same order of magnitude. Many factors concur to these discrepancies in a multi-step procedure as the flux estimation. Among these factors we mention possible different definition of the vector $\mathbf{k}$ in Eq. (4), $U_{10}$ in Eq. (18) or the definition of the pixel mask. Nevertheless, since the order of magnitude of the estimated flux in this work and in literature is the same (thousands of kg/h) we are confident that the applied procedure is correct. The usage of the MF-EVO algorithm leads to the following results: the average enhancements found are 0.68 ppm, 0.77 ppm and 0.67 ppm, which lead to fluxes of $2740 \pm 1140$ kg/h (that is -20% with respect to MF-Classic), $2890 \pm 1170$ kg/h (that is −41% with respect to MF-Classic) and $2200 \pm 900$ kg/h (that is −40% with respect to MF-Classic) respectively.

This discrepancy found between the MF-Classic and MF-EVO estimates is not surprising, as it is in line with the possible overestimation of the MF-Classic method for little concentration enhancements in heterogeneous backgrounds as noted in Section 3.1.

### 4.2. Widespread emission sources

The MF method can be successfully applied also for the identification of non-punctual sources, as long as the emission is significant. Among the real-world applications considered in this work, the Mumbai metropolitan landfills (India) represent an heterogeneous and challenging scenario. For this reason, they are used to quantitatively illustrate the impact on methane flux estimation of the log-domain approach, first on its own and then as part of the full processing chain (Section 5), which includes clustering homogenization. From information retrieved from the online press the Mulund dumping ground in Mumbai was closed as an active landfill in 2018 (Mulund, 2025). It is currently undergoing scientific disposal. The Kanjurmarg dumping ground is still open and handles about 80% of Mumbai's waste disposal needs. It remains the city's main landfill, processing the majority of its daily solid (Kanjurmarg, 2025). The Deonar Dumping Ground is still open and receives daily waste in 2025, despite official plans to close it (Deonar, 2025). In Fig. 6, the results of the application of the

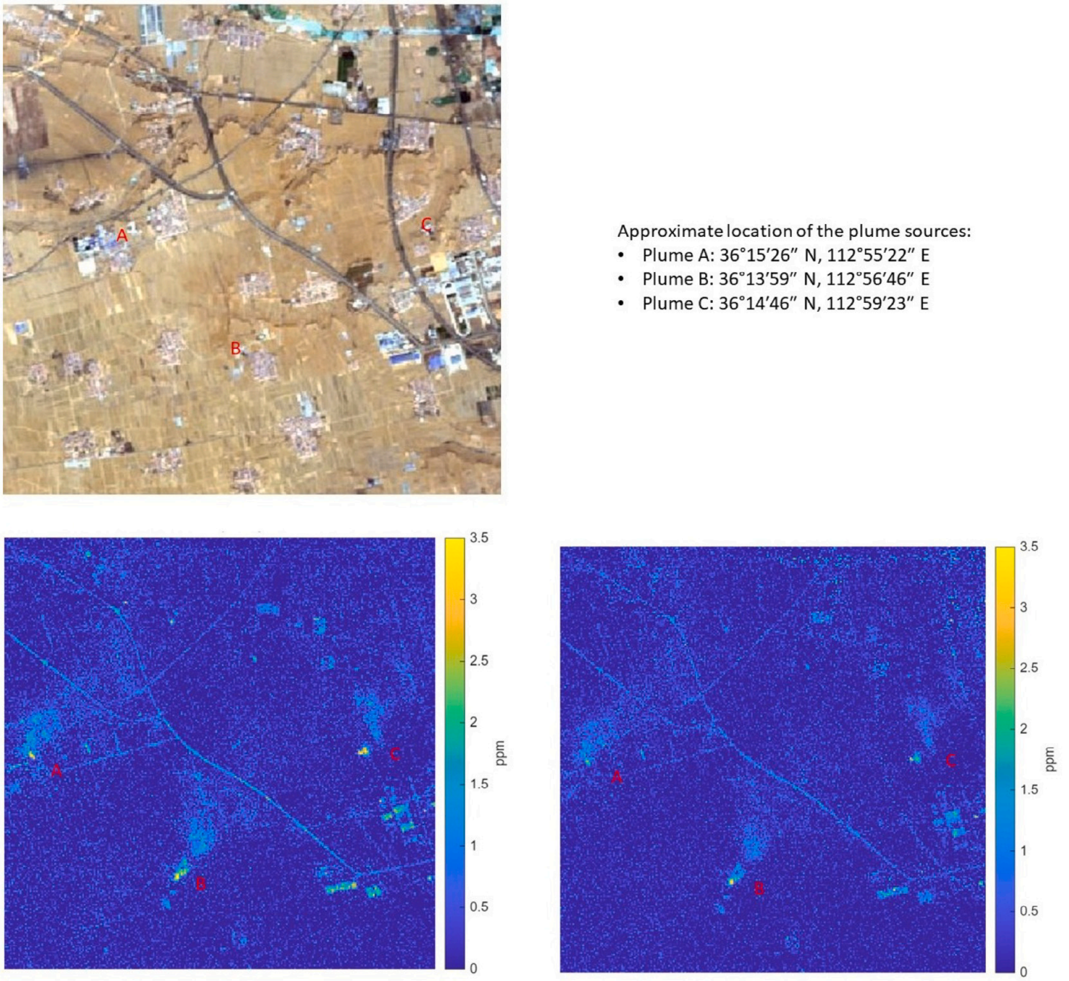

Approximate location of the plume sources:

- Plume A: 36°15′26″ N, 112°55′22″ E
- Plume B: 36°13′59″ N, 112°56′46″ E
- Plume C: 36°14′46″ N, 112°59′23″ E

**Fig. 5.** *Test on real data, China* - Top row: RGB composite of a PRISMA image taken over Coal Mines in the Shanxi region, China, on February 6, 2021. The approximate coordinates of the plumes sources are also indicated. Bottom row: corresponding $\Delta XCH_4$ maps obtained applying the MF-Classic (Left) and MF-EVO (Right).

MF-EVO method to PRISMA observations of the Mumbai Metropolitan Region (Agenzia Spaziale Italiana (ASI), 2025) are shown. The three signals highlighted in the $\Delta XCH_4$ maps, lie, in fact, in correspondence of the Mulund Dumping Ground, Kanjurmarg Dumping Ground and Deonar Dumping Ground (top to bottom), resulting in an average concentration enhancement of 1.22 ppm, 2.62 ppm and 1.71 ppm respectively. The three widespread sources do not provide any plume-like emission. However, the same steps described is Section 2.3 are used for the estimation of the fluxes. The results are: 1960 ± 980 kg/h (Mulund), 3900 ± 1955 kg/h (Kanjurmarg), and 5350 ± 2675 kg/h (Deonar).

## 5. Background homogenization strategy

The analyses presented in the previous sections demonstrate the intrinsic advantages of the MF-EVO formulation. However, when dealing with real hyper-spectral observations, an important source of uncertainty in methane enhancement and flux estimation arises from scene heterogeneity and not only from the matched filter formulation itself. For this reason, MF-EVO is implemented as part of a processing chain specifically designed to homogenize the background radiance and suppress methane-like false positives prior to flux estimation. In this work, we assume that degradation in methane enhancement and flux estimation can arise from the following factors:

1. **Methane-like absorbers:** pixels characterized by surface features that produce a signal in the $\Delta XCH_4$ map similar to an apparent methane enhancement relative to the background value;
2. **Reflectance heterogeneity:** regions with heterogeneous surface reflectance yield a mean background radiance that is not representative of a homogeneous scene, thus violating one of the fundamental assumptions of the MF algorithm;
3. **Elevation variations:** pixels located at different elevations introduce heterogeneity in the absorption path length, affecting MF results. This source of inhomogeneity is largely mitigated when using MF-EVO (presented in Appendix B);

The aforementioned sources of signal degradation are investigated in the following sections, where the proposed homogenization and preprocessing techniques are also discussed. In the following, we refer to the combination of MF-EVO, false-positive elimination, and scene partitioning as to "MF-EVO full chain". The results presented in the earlier sections do not include the clustering procedure or the false-alarm elimination step. These preprocessing algorithms are introduced only after evaluating the performance of MF-EVO on synthetic cases, which are designed to isolate and assess the algorithm's intrinsic behavior without the additional complexity of real-scene variability. When real scenes are analyzed, both MF-EVO and the classical MF benefit significantly from the application of clustering and false-alarm reduction procedures, which enhance detection reliability and reduce spurious responses. The

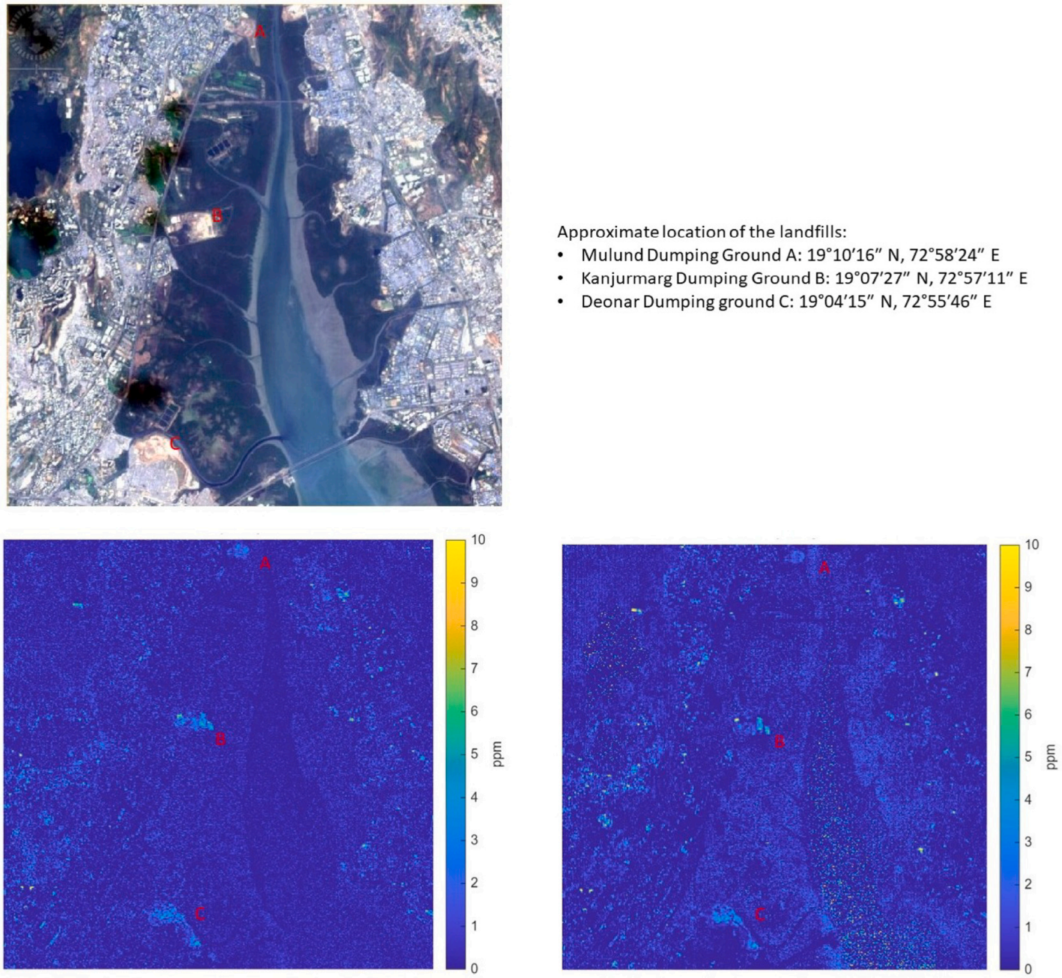

Approximate location of the landfills:

- Mulund Dumping Ground A: 19°10′16″ N, 72°58′24″ E
- Kanjurmarg Dumping Ground B: 19°07′27″ N, 72°57′11″ E
- Deonar Dumping ground C: 19°04′15″ N, 72°55′46″ E

**Fig. 6.** *Test on real data, India* - Top row: RGB composite of a PRISMA image on the Mumbai Metropolitan Region, India, taken on February 2, 2021. The approximate coordinates of the landfills are reported. Bottom row: corresponding $\Delta XCH_4$ maps obtained applying the MF-Classic (Left) and MF-EVO (Right).

outcome is a more accurately characterized background radiance (with reduced error) and, consequently, a less noisy $\Delta XCH_4$ map. Recently proposed approaches that modify the matched filter formulation itself, such as sparse-reconstruction-based methods (Li et al., 2025), address false alarms at the pixel level, whereas the present framework focuses on scene-level stabilization through modular preprocessing and background homogenization. Note that atmospheric conditions are always assumed to be homogeneous; therefore, PRISMA images affected by cloud or aerosol contamination or by strong variations in water vapor concentration are excluded from the analysis.

### 5.1. A-priori elimination of methane-like absorbers

The application of the MF benefits of a-priori information concerning the observed surface types. Since the performances of the MF algorithm increase in accordance with the increasing level of homogeneity of the scene, it is desirable to set up an algorithm capable of detecting surfaces which provide false alarms in the $\Delta XCH_4$ map. This pre-screening process aims at minimizing the inhomogeneity and improve the MF results. For typical PRISMA images, covering a squared area of 900 km$^2$, multiple surface types are usually present. It is then possible that surface spectral features, similar to those characterizing methane absorption, are present, providing a signal compatible with an increase in methane column concentration. As a result, false alarms, corresponding to positive $\Delta XCH_4$, appear on the map produced by the MF algorithm.

In case of large methane leakages originating from point sources, the produced emission is expected to have a plume-like behavior. While spurious signals from surface features may appear in the $\Delta XCH_4$ map, they do not significantly impede the overall detection capability. Our methodology maintains robust detection by relying on dual criteria: the magnitude of the $\Delta XCH_4$ and the conformity to the expected plume morphology. In these cases, it is common to adopt a pattern recognition algorithm for plume identification (Guanter et al., 2021). Nevertheless, in case of weak emissions or non-punctual sources, we expect that the increase in the $CH_4$ concentration in the air column provides a signal, in the $\Delta XCH_4$ maps, not strictly limited to a plume-like structure. In these situations, $CH_4$ concentration enhancements can be widespread over large areas or, otherwise, confined to individual pixels. Thus, the availability of a methodology to detect false alarms related to surface reflectance is critical to avoid misclassification. In addition, as the $\Delta XCH_4$ maps are derived by from a mean background radiance, which can be calculated considering the entire image (see Eqs. (3) and (14)), the more homogeneous is the target scene and the more accurate are the estimates of $\Delta XCH_4$ (Guanter et al., 2021).

As an example of a possible approach for scene homogenization, we consider the metropolitan city of Bologna, for which we opted to use a machine learning approach in the false alarm identification and mask. Results are shown in Fig. 7. First, we assess that two particular classes, constituted by solar panels and greenhouse plastic covers, produce strong signals in the $\Delta XCH_4$ maps (both MF-Classic and MF-EVO), which are compatible with a methane concentration increase.

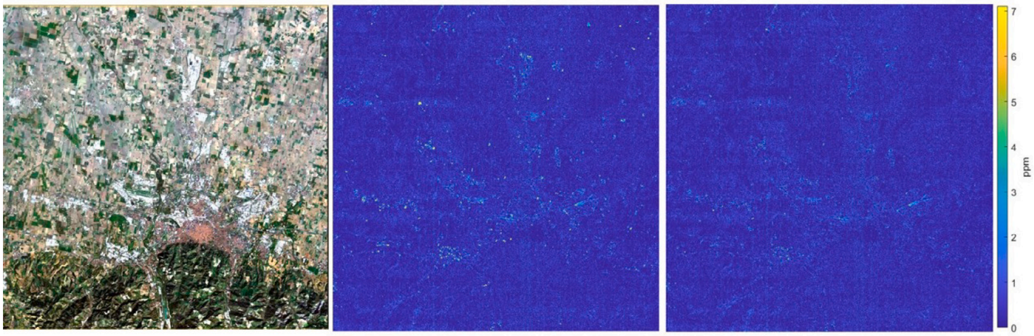

**Fig. 7.** *False Positive Elimination* - Left panel: RGB composite of the PRISMA image of Bologna Metropolitan Area, Italy. Center panel: $\Delta XCH_4$ map from the MF method. Right panel: $\Delta XCH_4$ with the exclusion of methane-like absorbers.

Both solar panels and greenhouses are very common in the Bologna province and their elimination from the $\Delta XCH_4$ maps facilitates both the search for methane sources, by making the background radiance more homogeneous, and the subsequent estimation of the methane enhancements. Hence, we train a Support Vector Machine (SVM) model to identify solar panels and greenhouses using the PRISMA reflectance spectral signature of the pixels as features. We use 47 pixels containing solar panels, 78 pixels containing greenhouses and 60 pixels, randomly chosen in the image, not belonging to the previous classes. The labeling was made by manual digitization, using as guidance high spatial resolution images, such as the ones available on Google Earth. As features, we adopt the reflectance spectra of the pixels in the spectral band 950–2100 nm, discarding the channels mainly affected by water vapor absorption (1360–1448 nm and 1803–1949 nm). We then compare the two most used decision rules (1vs1 and 1vsRest) in the extension of the SVM to multiclass classification: for our data, 1vsRest strategy yields the best results, but both decision rules allow a classification accuracy higher than 90%. In the right panel of Fig. 7 the impact of the elimination of false positive signals in the $\Delta XCH_4$ map of the Bologna metropolitan area is shown. By eliminating a significant number of pixels, the new $\Delta XCH_4$ map now provides a cleaner base for the study of the methane distribution in the considered area. Note that the classification procedure is not applied on the entirety of the pixels of the image, but only on those pixels with a $\Delta XCH_4$ value greater than $3\Sigma$, since the aim was not a thorough classification of the pixels but the identification of false positive cases. The improvements in background radiance homogenization, resulting from the application of the strategy, are reported in Table 6 where the first three moments of the distribution of $\Delta XCH_4$ are shown.

The homogenization procedure effectively reduces the standard deviation of the $\Delta XCH_4$ distribution. The initial positive skewness subsequently shifts toward zero, indicating that a population of strong positive artifacts has been removed, resulting in a more symmetric final distribution of estimated methane enhancements.

The SVM is used as a targeted, supervised false-positive suppression step within the processing chain and is not intended to provide exhaustive detection of all methane-like surface types; residual scene heterogeneity is subsequently addressed through clustering-based background homogenization (see next Section).

**Table 6**
Mean, Standard Deviation and Skewness of the $\Delta XCH_4$ maps, in the Bologna scenario, with and without the application of the a-priori false positive elimination strategy.

| *Moment* | *MF* | *MF without false positives* |
|---|---|---|
| Mean | ~ 0 | ~ 0 |
| Standard Deviation | 0.99 | 0.94 |
| Skewness | 0.72 | 0.17 |

### 5.2. Background homogenization by means of scene partition

The efficiency of the MF is also affected by the level of homogeneity of the observed scene. Heterogeneity in the surface reflective properties provides variability in the background pixel radiance values which results in a 'noisy' $\Delta XCH_4$ map, thus lowering both the capability to identify the methane source and to estimate the corresponding concentration enhancement. To avoid degradation of the methane sources identification and of the quantification of the concentration enhancements we propose to increase the homogeneity of the scene by its partition. The basic idea is to avoid the application of the MF to the whole PRISMA image as usual. Instead, the image is partitioned into a limited number of homogeneous subsets, for which the surface reflectance is approximately the same. The MF is then applied to each single homogeneous subset of the image and the methane sources are searched within the partitioned areas of the image instead of the full image at once. The implementation of the MF method on homogeneous subsets of pixels comes at the cost of adopting an algorithm for the selection of the homogeneous areas in the image. Furthermore, it requires a number of runs of the MF code for each homogeneous subset which is identified. Our strategy consists of selecting homogeneous subsets by running clustering routines applied to the L2C PRISMA reflectance product (the bottom of atmosphere reflectance Agenzia Spaziale Italiana (ASI), 2020). The reflectance values considered refer to channels that are not correlated to the ones used by the MF, namely the VNIR hypercube (400–950 nm). Several clustering strategies are tested including Hard Clustering, Fuzzy Clustering and Spectral angle Mapper. We decided to adopt an unsupervised method, the Mixture of Gaussians method (Kambhatla and Leen, 1994), for its simple applicability and excellent results. Before the application of the method, a simple normalization of all the pixel surface spectral reflectance $r_i$ is performed by using the formula:

$$r_{i,ca} = \frac{r_{i,PRISMA}}{\sum_{n=1}^{nc} r_{n,PRISMA}} \tag{19}$$

where $r_{i,ca}$ is the reflectance value at the $i$th channel used in the clustering algorithm, $r_{i,PRISMA}$ is the spectral reflectance as provided by PRISMA L2C products and $nc$ is the total number of channels used in the clustering algorithm. The number of classes adopted is scene dependent and should correspond to the minimum number capable to describe the main features of the scene. As examples, in Figs. 8 and 9 the clusterization of the PRISMA observations already reported in Figs. 5 and 6 are shown. For both cases, five classes are considered to properly describe the scenes.

The result of the clusterization is twofold since it allows to run the MF algorithm on pixels pertaining to a single cluster or, possibly, to

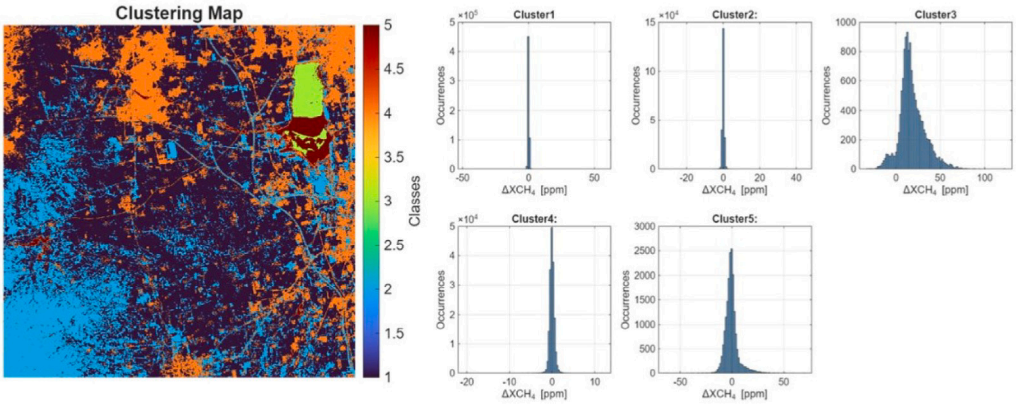

**Fig. 8.** Clusterization of the PRISMA image over Coal Mines in the Shanxi region, China, on February, 6, 2021 (a part of which is shown in Fig. 5). Left panel: Clustering map of the classes: Dark blue — Bright terrains, Light Blue — Dark terrains, Green — Deep water, Orange — Bright areas (e.g. clouds) and urban areas, Red - Shallow water and mud. Right panel: $\Delta$XCH$_4$ pixel distribution for each of the 5 classes shown in the left panel. (For interpretation of the references to color in this figure legend, the reader is referred to the web version of this article.)

**Fig. 9.** *Image Clusterization, India* - Left panel: RGB composite of the Mumbai Metropolitan Region, India, total image. Right panel: Clustering map of the considered scene. Classes: Dark blue — Bright terrain and residential areas, Light Blue — Water, Green — Shoreline terrain and densely populated urban areas and roads, Orange — Black spots, Red — Vegetation. (For interpretation of the references to color in this figure legend, the reader is referred to the web version of this article.)

exclude pixels referring to clusters which are considered detrimental for the methane search. For the China case study, the clustering map shown in Fig. 8 is complemented by histograms of the associated methane enhancements for each of the five identified surface classes. Pixels belonging to clusters 3 and 5, corresponding to water and mud surfaces, exhibit the largest spread and pronounced asymmetry in the $\Delta X\mathrm{CH}_4$ distributions; for this reason, they are excluded from the analysis. The impact of applying the full processing chain (MF-EVO combined with background homogenization), compared with the simple application of MF or MF-EVO alone to the PRISMA image, is assessed in Table 7. When the full MF-EVO chain is used instead of MF alone, reductions larger than 50% in the estimated emission fluxes are observed for all plumes. These reductions are primarily driven by the markedly different spectral behavior of water and mud surfaces compared to sand (or other bright surfaces), which constitute the majority of the image. Similar results are obtained for the case study referred to the Mumbai area that is reported in Figs. 9 and 10. Also in this case the water surfaces cover large part of the observations and potentially affect the methane source identification and flux estimation (due to the very low reflectivity of water). The exclusion of water pixels from the $\Delta$XCH$_4$ computation improves the accuracy of the estimate of the background radiance and improves the quality of the map as shown in Fig. 10. Results obtained after scene partition differ from estimates assuming the background radiance from averaging over the full image. For the India case, the estimated $\Delta$XCH$_4$, using MF-EVO, and the resulting fluxes are: 0.75 ppm and $1210 \pm 615$ kg/h (Mulund), 1.64 ppm and $2450 \pm 1230$ kg/h (Kanjurmarg), 0.98 ppm and $3060 \pm 1530$ kg/h (Deonar). In Table 8 a summary of the estimated fluxes obtained for the three landfills in the Mumbai area is provided when using MF-Classic, MF-EVO and MF-EVO with the exclusion of water surfaces (MF-EVO full chain). This last case, which is our best flux estimate, provides values significantly lower than the estimates obtained using the MF Classic algorithm. Additional examples of methane enhancements and flux emission estimates from real data are provided in Appendix C. These results suggest that, for heterogeneous environments, advances in methane retrieval accuracy depend at least as much on scene-level pre-processing and homogenization as on the choice of the matched filter formulation. In this context, the reduction of 40%–55% observed with respect to the classic MF applied to the full scene cannot be attributed to the MF-EVO formulation alone, but emerges from the full processing chain. Across the different real-world applications presented in this study, the proposed processing chain consistently improves the spatial

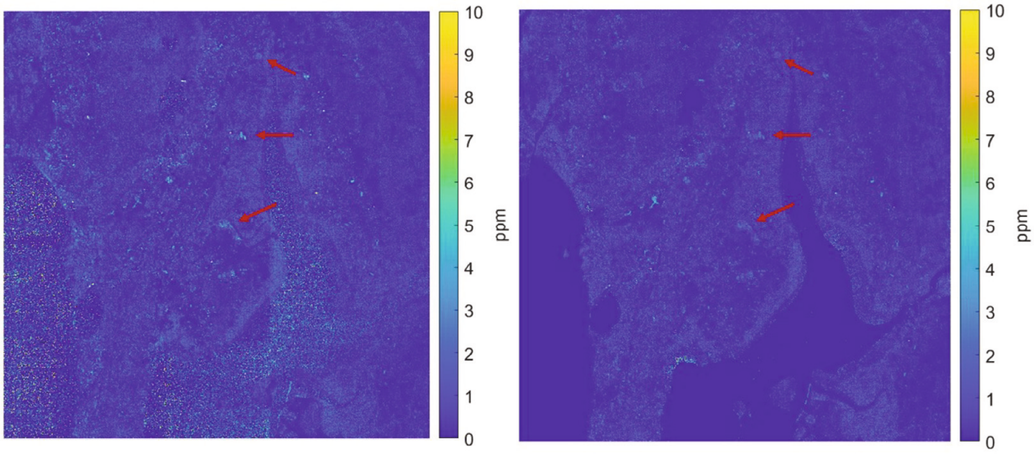

**Fig. 10.** *Elimination of water surfaces* - $\Delta XCH_4$ map of the Mumbai Metropolitan Area using the MF-EVO. Left panel: no clusterization is applied. Right panel: the $\Delta XCH_4$ map is obtained excluding class number 2 (water) of Fig. 9. With the red arrows, the three landfills are highlighted, as in Fig. 6. (For interpretation of the references to color in this figure legend, the reader is referred to the web version of this article.)

**Table 7**
Coal Mines in Shanxi Region, China. Estimated fluxes [kg/h] using MF-Classic, MF-EVO and MF-EVO excluding water pixels in the computation of the methane enhancements.

| | *MF-Classic* | *MF-EVO* | *MF-EVO full chain* |
|---|---|---|---|
| Plume A | 3820 ± 1540 | 2740 ± 1140 | 1750 ± 760 |
| Plume B | 4075 ± 1640 | 2890 ± 1170 | 1810 ± 880 |
| Plume C | 3090 ± 1250 | 2200 ± 900 | 1490 ± 620 |

**Table 8**
Mumbai Metropolitan Region, India. Estimated fluxes [kg/h] using MF-Classic, MF-EVO and MF-EVO excluding water pixels in the computation of the methane enhancements.

| | *MF-Classic* | *MF-EVO* | *MF-EVO full chain* |
|---|---|---|---|
| Mulund | 2620 ± 1310 | 1960 ± 980 | 1210 ± 620 |
| Kanjurmarg | 4360 ± 2200 | 3900 ± 1960 | 2450 ± 1230 |
| Deonar | 5340 ± 2670 | 5350 ± 2680 | 3060 ± 1530 |

coherence of methane enhancement maps and reduces background-driven artifacts relative to the classical MF. While the magnitude of the impact varies depending on scene heterogeneity and source geometry, the results demonstrate that the benefits of background homogenization and false-positive suppression are not limited to a single case study, but extend across diverse environmental and observational conditions.

Finally we note that the application of the MF routine on homogeneous areas improves the identification of methane sources and eventually the estimate of $\Delta XCH_4$, but the recombination of the results of the different classes into a single $\Delta XCH_4$ map becomes challenging as different areas show enhancements relative to different background values.

## 6. Conclusions

This study discusses the physical foundations of the Matched Filter methodology which is widely applied to hyper-spectral satellite imagers' observations for the identification of the methane sources and it is at the base of the computation of the estimation of the concentration enhancements. The alternative log-domain formalization of the method (here named MF-EVO), which accounts for a estimator of the methane concentration enhancement working in the optical depth domain, is examined. MF-EVO considers the rate of change of the two-way spectral transmissivity resulting from a methane concentration increase along the light path and uses the precomputed optical depth for a unit concentration increase, which is weighted over the covariance matrix of optical depth variation with respect to the background value. The implementation of the algorithm is straightforward and the running time is equivalent to the classical methodology.

When applied to idealized conditions, created using simulated observations of the Italian Space Agency sensor PRISMA, the MF-EVO outperforms the classical Matched Filter (MF-Classic). Specifically, we demonstrated that MF-EVO is less sensitive to sensor noise by providing a narrower distribution of the $\Delta XCH_4$ for homogeneous background conditions, thus improving the detectability of methane sources with respect to the classical Matched Filter. We estimate that, in idealized conditions (uniform background), the identification limits for MF-EVO and MF classic are, respectively, $\Delta XCH_4 = 0.05$ ppm and $\Delta XCH_4 = 0.09$ ppm.

The estimation of the methane concentration enhancement is also improved by using the MF-EVO. For a homogeneous background, the two methods perform equivalently when methane concentration enhancements are smaller than 5 ppm, but MF-EVO is more accurate for larger enhancements with errors lower than 1% for the larger emission case considered (20 ppm), compared to errors of the order of 20% for the classical methodology under the same conditions. Simulations in the presence of a composite background show that the classic Matched Filter $\Delta XCH_4$ retrievals are affected by errors up to approximately 50% for methane concentration enhancements limited to 1 ppm and 20% when enhancement are of 20 ppm. For the same conditions, MF-EVO provides results with errors less than 5% (for any methane increase), which is promising for its application to real cases that are usually heterogeneous.

The application of MF-EVO to real PRISMA observations provides results consistent with previous findings obtained using the classical methodology. It is also demonstrated that MF-EVO is successfully applied to the identification of widespread methane emissions such as extended landfills. The comparison between the two methodologies aims to quantify the practical benefits of the MF-EVO approach in real-world applications. Crucially, we observe no significant difference in plume/emission detection capabilities for the two cases analyzed, but we highlight notable variations in flux estimations, which stem predominantly from the distinct enhancement levels calculated within the plume pixels by each method.

When dealing with real data, it is well known that the process used for the identification of methane sources is made difficult by the large number of features that are usually present in the image and degrade the $\Delta XCH_4$ maps. The causes are varied and include heterogeneity in the surface reflectance (including surfaces with absorption spectral features similar to methane) and elevation variations over the observed image. These two causes are investigated and some strategies are provided to eliminate methane enhancements false alarms, homogenize the observed scene by considering a partitioning over which the Matched Filter is run (which implies excluding surfaces such as water) and, eventually, correct the differences in pixel altitudes which might affect the evaluation of the proper background radiance and of the $\Delta XCH_4$ estimates. Examples of the application of these strategies to PRISMA data are presented for two case studies: one involving point methane sources in China and another involving extended sources in India. For both cases, the complete processing chain is demonstrated, showing that methane flux estimates obtained with the full MF-EVO chain (log-domain matched filtering and scene homogenization) are lower than those derived using the classical method as well as MF-EVO alone. The impact of the full processing chain is particularly evident in the application to the Mumbai metropolitan landfills. When background homogenization through scene partitioning and false-positive suppression are applied in combination with MF-EVO, the resulting methane flux estimates are reduced by approximately 40%–55% compared to those obtained using the classic MF applied to the full scene. This difference highlights the dominant role of background characterization and scene heterogeneity in flux estimation for widespread sources, and demonstrates that methodological choices beyond the matched filter formulation itself can strongly influence quantitative emission estimates.

A systematic comparison of the proposed processing chain with alternative retrieval approaches, together with validation against independent surface-based measurements (e.g. ICOS stations, facility-level surveys, and field campaign data), constitutes a natural next step of this work. Such comparisons will be necessary to better quantify the accuracy of the derived flux estimates under different environmental conditions and to identify possible directions for further methodological improvements. In this context, future studies will focus on the use of coordinated satellite and ground-based observations to support validation and refinement of the proposed approach.

## CRediT authorship contribution statement

**Fabrizio Masin:** Writing – original draft, Visualization, Software, Investigation, Formal analysis. **Tiziano Maestri:** Writing – review & editing, Supervision, Methodology, Funding acquisition, Conceptualization. **Michele Martinazzo:** Validation, Methodology, Investigation. **Giorgia Proietti Pelliccia:** Software.

## Declaration of competing interest

The authors declare that they have no known competing financial interests or personal relationships that could have appeared to influence the work reported in this paper.

## Acknowledgments

The authors acknowledge Dr. Simona Zoffoli, Dr. Patrizia Sacco and Dr. Lopinto Ettore of the Italian Space Agency (ASI) for the support and the provision of PRISMA data (Agenzia Spaziale Italiana (ASI), 2025). We thank Prof. Paolo Garofalo of University of Bologna for the valuable discussions. We also thank the reviewers for their thoughtful comments and suggestions.

## Appendix A. Formal derivation of the matched filter

A matched filter is a linear operator tuned to detect a signal hidden within noisy data. This is generally performed by maximizing the signal to noise ratio (SNR) of the data. In our problem, the signal to extract is the methane signature within the radiance measurement collected by the PRISMA satellite. Given the expansion for the theoretical observed radiances (Eq. (1)):

$$I \simeq I(r_0, \rho_0) + \frac{\partial I}{\partial r}\Delta r + \frac{\partial I}{\partial \rho}\Delta \rho \tag{A.1}$$

Where $r$ is the surface reflectivity and $\rho$ is the methane concentration. We can assume that the satellite will measure a quantity ($I_p$) in the presence of the methane plume:

$$I_p = I + \epsilon \tag{A.2}$$

Where $\epsilon$ is an additive unbiased Gaussian noise, not correlated with the measurement. Assuming a neglectable effect of the surface reflectivity, we are interested in extracting the signature of the methane change, $\rho_p$, with respect to the background $I(r_0, \rho_0)$. To do so, we can define the quantity $x$:

$$x = I_p - I(r_0, \rho_0) = \frac{\partial I}{\partial \rho}\rho_p + \epsilon = t\rho_p + \epsilon \tag{A.3}$$

and create a linear operator $M$ such that the quantity $y = x^T M$ has the maximum signal to noise ratio. Starting from the definition of SNR:

$$SNR = \frac{|\rho_p \cdot t^T M|^2}{E[|\epsilon^T M|^2]} \tag{A.4}$$

With $E[\cdot]$ the expectation value. Now, noting that $E[\epsilon\epsilon^T] = \Sigma$ is the covariance matrix of the noise, the SNR can be written as:

$$SNR = \frac{|\rho_p \cdot t^T M|^2}{M^T \Sigma M} = \frac{\rho_p^2 |(\Sigma^{1/2} M)^T (\Sigma^{-1/2} t)|^2}{(\Sigma^{1/2} M)^T (\Sigma^{1/2} M)} \tag{A.5}$$

And, exploiting the Cauchy–Schwarz inequality:

$$\begin{aligned} \frac{\rho_p^2 |(\Sigma^{1/2} M)^T (\Sigma^{-1/2} t)|^2}{(\Sigma^{1/2} M)^T (\Sigma^{1/2} M)} &\leq \frac{\rho_p^2 [(\Sigma^{1/2} M)^T (\Sigma^{1/2} M)][(\Sigma^{-1/2} t)^T (\Sigma^{-1/2} t)]}{(\Sigma^{1/2} M)^T (\Sigma^{1/2} M)} \\ &= \rho_p^2 \cdot t^T \Sigma^{-1} t \end{aligned} \tag{A.6}$$

This represent an upper bound that is reached when:

$$M = c \cdot \Sigma^{-1} t \tag{A.7}$$

With $c$ a constant value. The explicit value for this constant can be found by asking that:

$$E[|y|^2] = c^2 \cdot E[|x^T \Sigma^{-1} t|^2] = \rho_p^2 \tag{A.8}$$

Which is found when:

$$c = \frac{1}{t^T \Sigma^{-1} t} \tag{A.9}$$

It follows that our final form for the matched filter will be:

$$M = \frac{\Sigma^{-1} t}{t^T \Sigma^{-1} t} \tag{A.10}$$

From which:

$$\rho_p = \frac{(I_p - I(r_0, \rho_0))^T \Sigma^{-1} t}{t^T \Sigma^{-1} t} \tag{A.11}$$

It is important to note that, in defining the quantity $x$, we implicitly assume that the background radiance $I(r_0, \rho_0)$ is known exactly. However, in practical applications, this value is not known and must be estimated from the scene. In general, the definition of the background radiance is subjected to errors $\tilde{\epsilon}$, leading to the following form of $x$:

$$x = I_p - I(r_0, \rho_0) + \tilde{\epsilon} = t\rho_p + \epsilon + \tilde{\epsilon} \tag{A.12}$$

A correct derivation of the matched filter requires an effective description of error terms, which should be Gaussian and unbiased with

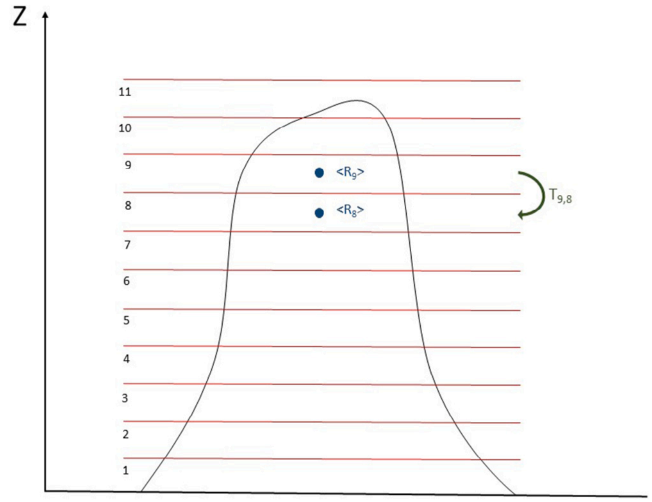

**Fig. B.1.** *Transmissivity correction* - Qualitative description of the cascade transmissivity correction method described by Eq. (B.1).

respect to the quantity $x$. Although this is assumed to be true for $\epsilon$, this could not be the case for $\tilde{\epsilon}$. To preserve the validity of the mathematical framework, the following condition must therefore be satisfied:

$$\tilde{\epsilon} \ll \epsilon \tag{A.13}$$

This can be achieved by removing spurious elements from the background radiance computation and by applying the homogenization of the observed scene. Similar considerations apply to other sources of uncertainties. These could include errors in the definition of $t$, due profile assumptions.

## Appendix B. Effect of surface elevation and correction methods

The topography of the terrain can constitute a source of background inhomogeneity that adds to the natural variations in surface reflectivity within the observed scene. For example, in the presence of surface altitude inhomogeneity within the PRISMA image, the path traveled by the incident and reflected solar light can significantly affect the radiance attenuation in accordance with the surface altitude. For low altitude surfaces the sunlight absorption in the methane bands is increased with respect to what happens to pixels referring to high altitude regions in the image. In this section we limit our analysis to the effect of surface altitude changes within the image and do not include corrections for broader topographic or orographic influences, such as terrain-induced heterogeneities in viewing geometry. While topographic and orographic effects can introduce additional uncertainties, their explicit treatment lies outside the scope of this work and is therefore acknowledged as a limitation.

Our strategy to study the effect of elevation on the MF products is to assume a scenario in which the background surface is split into two different areas characterized by the same surface type (assumed woods for this case) and different altitude levels. In these background conditions three patches of strong methane enhancement (5 ppm, 10 ppm and 20 ppm) are simulated. The aim of this analysis is to investigate the impact of surface altitude inhomogeneity on the derived $\Delta XCH_4$ estimates, also through a comparison with the results presented in Section 3.2 where an homogeneous surface at sea level was assumed.

The layout of the analysis follows the configuration shown in the left column of Fig. 3. The scene is horizontally divided into two parts: the first two patches are located in the upper portion of the image, while the third one is in the lower portion. The background reflectivity is of the same type in both regions; however, one region is assumed to be at an altitude of 0 m above sea level, whereas the other half is set at different altitude steps of 300 m, 500 m, 750 m, and 1000 m a.s.l.

**Table B.9**
Derived methane enhancements concentration (in ppm) using MF-Classic and MF-EVO for three patches when considering the background affected by altitude heterogeneity, compared to the results for an homogeneous scenario at 0 m a.s.l. The assumed surface reflectivity is that one of “woods”.

| | *300* m | *500* m | *750* m | *1000* m | *uniform 0* m |
|---|---|---|---|---|---|
| | | | MF EVO trend | | |
| *5* ppm | 5.0 | 5.07 | 5.12 | 5.14 | 4.76 |
| *10* ppm | 10.0 | 10.13 | 10.24 | 10.28 | 9.56 |
| *20* ppm | 19.6 | 19.7 | 19.7 | 19.8 | 19.1 |
| | | | MF Classic trend | | |
| *5* ppm | 5.0 | 4.90 | 4.85 | 4.77 | 5.01 |
| *10* ppm | 9.18 | 9.20 | 9.09 | 8.91 | 9.29 |
| *20* ppm | 15.5 | 15.2 | 14.7 | 14.0 | 16.0 |

Simulations at various altitude steps are performed to assess whether any trend can be observed in the estimated enhancements for the patches located in the 0 m a.s.l. region. The results in Table B.9 show that MF-EVO is less sensitive to variation of the surface altitude in the image with respect to MF-Classic: in the EVO case, there is a slight positive shift as the altitude step increases, although the estimates remain generally consistent with the reference values. In the Classic case, a slight negative shift is observed, which increases in situations involving the large enhancements considered.

Our strategy aims at homogenizing the scene by rescaling all the radiances to the point of lowest altitude. The detected radiance, for each pixel, is corrected by using a parametric function of the altitude difference between the considered pixel and the lowest altitude point in the image. To achieve this, three different approaches are suggested:

- A physically based method exploits the knowledge, for each pixel, of the Sun zenith angle, of the viewing zenith angle (available in the PRISMA metadata) and of altitude of the pixels (to be derived after a map geolocation is performed). The information is used to compute an additional two-way transmissivity of the atmosphere along the path through a line-by-line radiative transfer code (such as lblRTM, 2023) for each specific pixel. The assumed gas concentration profiles depend on the availability of data or are assumed to be in their climatological values easily derived from climatological dataset (Remedios et al., 2007). At the end of the process all the spectral radiances measured by the sensor are corrected by a two-way transmissivity which is dependent on the pixel altitude and on the observational conditions.
- A data-driven method associates the observed pixels to various layers based on their geolocated surface altitude. Assuming that there are no variations in the surface reflectivity with the surface altitude level, the method computes the correction parameter between two contiguous layers as the reciprocal of the ratio between the average radiance value of the pixels in the layers (Fig. B.1). In particular:

$$\frac{1}{T_{n,n-1}} = \frac{\langle I_n \rangle}{\langle I_{n-1} \rangle} \tag{B.1}$$

where $T_{n,n-1}$ is the correction parameter used to multiply the pixels in layer n to homogenize them to the pixels in layer n-1. It represents a mean 2-way transmissivity between two consecutive layers. $\langle I_n \rangle$ and $\langle I_{n-1} \rangle$ are the average radiance values of the pixels laying at altitudes typical of layers n and n-1, respectively. The final goal is to apply a correction which normalizes all the pixel radiances to values as if they were at the same lowest altitude in the image. The pixels belonging to the layer n are multiplied by the n-1 parameters $T_{n,n-1}$, $T_{n-1,n-2}$, …, $T_{2,1}$, the pixels belonging to the layer n-1 are multiplied by the n-2 parameters

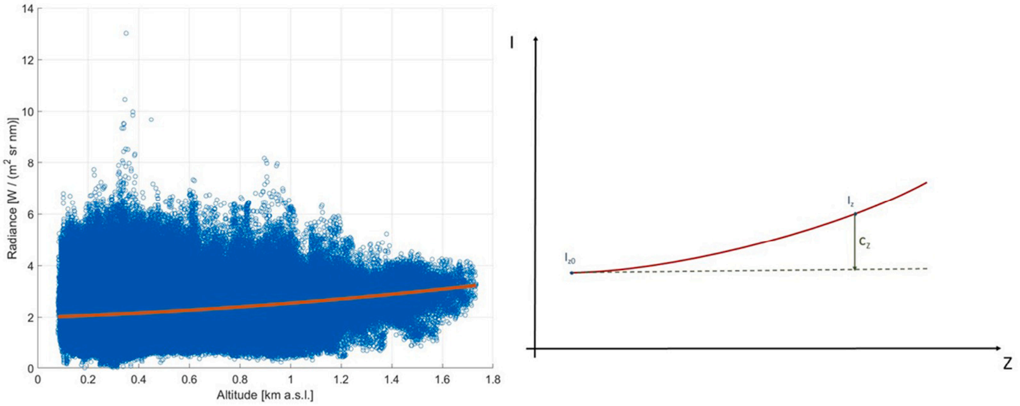

**Fig. B.2.** *Curve Fitting* - Curve fitting correction method for a scene centered on Mount Amiata, a mountain region in the center of Italy. Left: PRISMA radiances (at channel centered at 2053 nm) of all the pixels versus their altitude (blue circles). In red it is plotted the line fit obtained by a second order polynomial curve. Right: Depiction of the correction coefficient described in Eq. (B.1). (For interpretation of the references to color in this figure legend, the reader is referred to the web version of this article.)

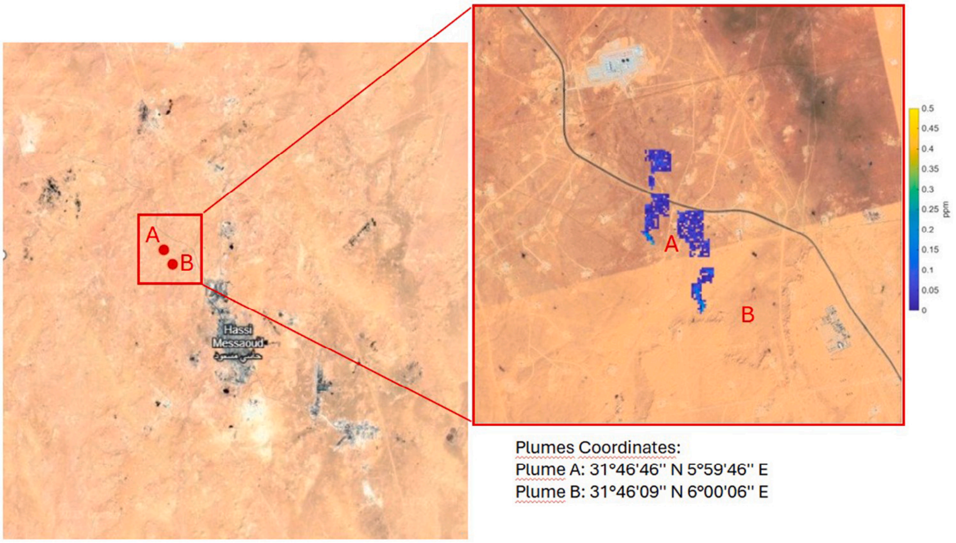

Plumes Coordinates:
Plume A: 31°46'46'' N 5°59'46'' E
Plume B: 31°46'09'' N 6°00'06'' E

**Fig. C.3.** Images of Hassi Messaoud Oil Fields, Algeria, referring to a PRISMA observation taken on August 30, 2020. The $\Delta$XCH$_4$ of the detected plumes, as resulting after the application of the MF-EVO full chain, are superimposed to the Google Earth image of the area.

$T_{n-1,n-2}$, $T_{n-2,n-3}$, …, $T_{2,1}$, and so forth. The methodology has the advantage to link the computation of the correctional parameter to the actual measurements of the observed scene instead of computing it from synthetic simulations.

- A statistically based method derives the polynomial curve fitting of the altitude vs. radiance graph (Fig. B.2 Left panel), which allows to find the correctional coefficients used to normalize the pixel radiance values to those of the lowest altitude level in the scene (Fig. B.2 Right panel). Specifically:

$$c_z = \frac{I_{z_0}}{I_z} \tag{B.2}$$

where $c_z$ is the correctional coefficient for the pixels at altitude z and $I_{z0}$ and $I_z$ are the radiance values at the lowest altitude in the scene and at altitude z.

Note that the described procedures are applied to each channel used in the matched filter method. The three methodologies are strictly valid only for homogeneous surfaces. Their application is suggested for images affected by significant variations in surface altitude but characterized by homogeneous reflective properties of the surfaces.

## Appendix C. Additional real-word cases

Three additional scenes observed by PRISMA (Agenzia Spaziale Italiana (ASI), 2025) are analyzed. The selected scenes are:

- two plumes in the Hassi Messaoud Oil Field in Ouargla Province, Algeria. The $\Delta$XCH$_4$ of the two plumes (named A and B) are

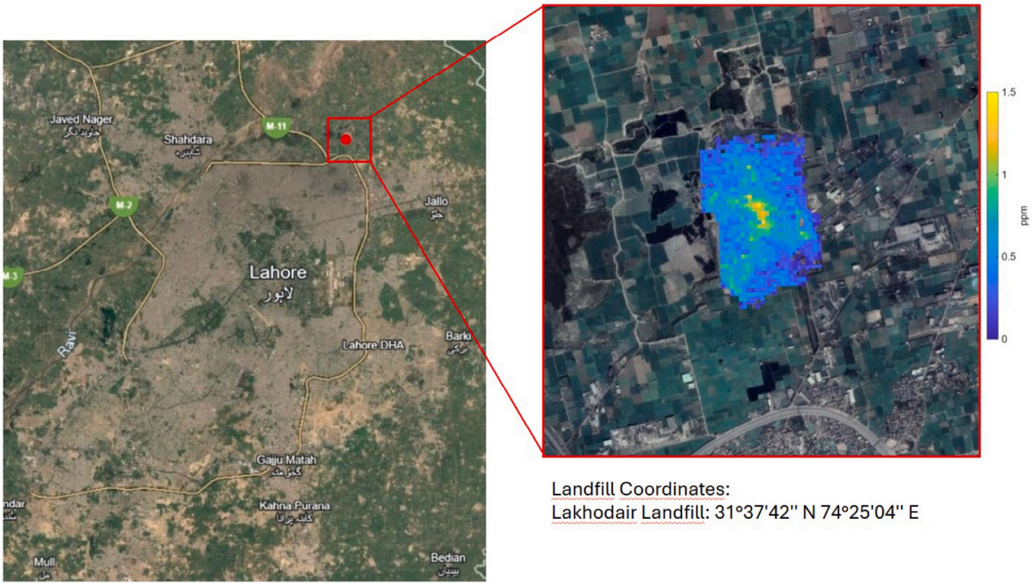

Landfill Coordinates:
Lakhodair Landfill: 31°37'42'' N 74°25'04'' E

**Fig. C.4.** Images of Lakhodair Landfill in Lahore, Pakistan, referring to a PRISMA observation taken on April 14, 2022. The analyzed $\Delta XCH_4$, as resulting after the application of the MF-EVO full chain, is superimposed to the Google Earth image of the area in the right panel.

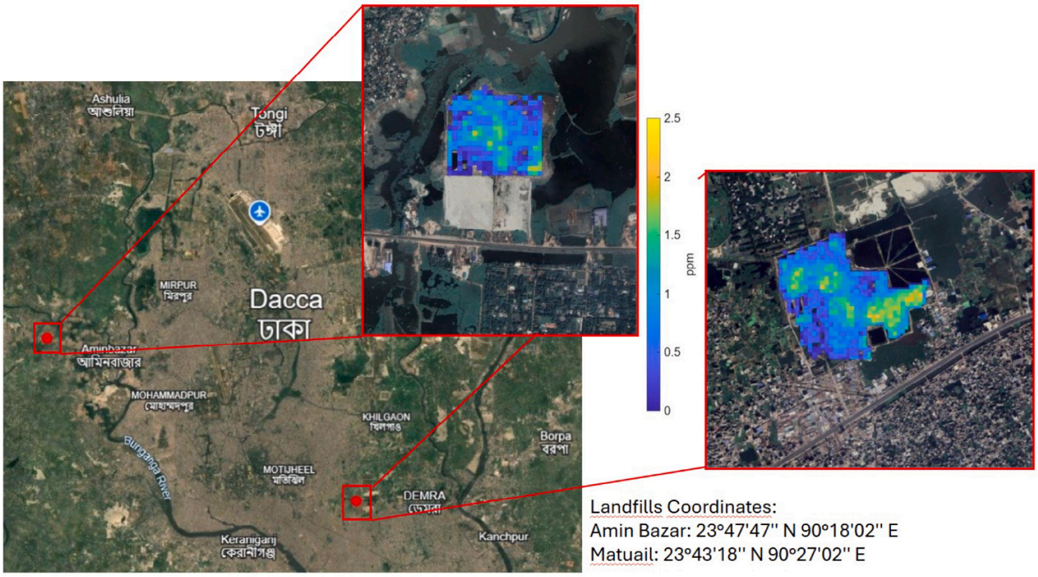

Landfills Coordinates:
Amin Bazar: 23°47'47'' N 90°18'02'' E
Matuail: 23°43'18'' N 90°27'02'' E

**Fig. C.5.** Images of Amin Bazar Waste Disposal Area and Matuail Waste Treatment Plant in Dhaka, Bangladesh, referring to a PRISMA observation taken on May 3, 2024. The two analyzed $\Delta XCH_4$, as resulting after the application of the MF-EVO full chain, are superimposed to the Google Earth image of the area in the right panel.

**Table C.10**
Summary of the fluxes [kg/h] estimated for the five emission analyzed.

| | *MF-Classic* | *MF-EVO* | *MF-EVO full chain* |
|---|---|---|---|
| Algeria, Hassi Massoud Plume A | 540 ± 300 | 260 ± 150 | 100 ± 60 |
| Algeria, Hassi Massoud Plume B | 600 ± 360 | 320 ± 200 | 120 ± 70 |
| Pakistan, Lakhodair | 2340 ± 1310 | 1940 ± 1110 | 1180 ± 680 |
| Bangladesh, Amin Bazar | 3180 ± 1750 | 2770 ± 1550 | 1560 ± 840 |
| Bangladesh, Matuail | 2830 ± 1720 | 2780 ± 1670 | 1850 ± 1130 |

superimposed to a Google Earth image of the area in the right panel of Fig. C.3;
- Lakhodair Landfill in Lahore, Pakistan. As in the previous case the scene is described in Fig. C.4;
- Amin Bazar Waste Disposal Area and Matuail Waste Treatment Plant in Dhaka, Bangladesh (Fig. C.5)

To the 3 cases we applied the Classic MF, the MF-EVO and the MF-EVO full chain and estimated the emitted fluxes. The results are reported in Table C.10, similarly to what done in Tables 7 and 8 for the China and India scenes.

## Data availability

Data will be made available on request.

## References

Agenzia Spaziale Italiana (ASI), 2020. PRISMA products specification document – Issue 2.3.

Agenzia Spaziale Italiana (ASI), 2025. PRISMA hyperspectral images. Available at: https://prisma.asi.it/. (Accessed: 14 March 2025). ID China: PRS_L1_STD_20210206031837_20210206031842_0001.he5 ID India: PRS_L1_STD_20210203054720_20210203054724_0001.he5 ID Bologna: PRS_L2C_STD_20201107101613_20201107101618_0001.he5 ID Algeria: PRS_L1_STD_20200830103014_20200830103018_0001.he5 ID Lahore: PRS_L1_STD_20220414054629_20220414054633_0001.he5 ID Dhaka: PRS_L1_STD_20240503044154_20240503044158_0001.he5.

Agusti-Panareda, A., Diamantakis, M., Bayona, V., Klappenbach, F., Butz, A., 2017. Improving the inter-hemispheric gradient of total column atmospheric CO2 and CH4 in simulations with the ECMWF semi-Lagrangian atmospheric global model. Geosci. Model. Dev. 10, 1–18. http://dx.doi.org/10.5194/gmd-10-1-2017.

Aumann, H.H., Chahine, M.T., Gautier, C., Goldberg, M.D., Kalnay, E., McMillin, L.M., Revercomb, H., Rosenkranz, P.W., Smith, W.L., Staelin, D.H., Strow, L.L., Susskind, J., 2003. AIRS/AMSU/HSB on the Aqua mission: design, science objectives, data products, and processing systems. IEEE Int. Geosci. Remote. Sens. Symp. 41 (2), 253–264. http://dx.doi.org/10.1109/TGRS.2002.808356.

Ayasse, A.K., Dennison, P.E., Foote, M., Thorpe, A.K., Joshi, S., Green, R.O., Duren, R.M., Thompson, D.R., Roberts, D.A., 2019. Methane mapping with future satellite imaging spectrometers. Remote. Sens. 11 (24), URL https://www.mdpi.com/2072-4292/11/24/3054.

Borchardt, J., Gerilowski, K., Krautwurst, S., Bovensmann, H., Thorpe, A.K., Thompson, D.R., Frankenberg, C., Miller, C.E., Duren, R.M., Burrows, J.P., 2020. Detection and quantification of ch4 plumes using the wfm-doas retrieval on aviris-ng hyperspectral data. Atmospheric Meas. Tech. Discuss. 2020, 1–34, URL https://amt.copernicus.org/preprints/amt-2020-275/.

Buono, A., Zaccardo, I., D'Amico, F., Lapenna, E., Cardellicchio, F., Laurita, T., Amodio, D., Colangelo, C., Di Fiore, G., Giunta, A., et al., 2025. Expanding continuous carbon isotope measurements of CO2 and CH4 in the Italian ICOS atmospheric consortium: First results from the continental POT station in potenza (Basilicata). Atmosphere 16 (8), 951. http://dx.doi.org/10.3390/atmos16080951, 2025.

CEOS, 2025. https://ceos.org/ourwork/workinggroups/climate/ghg-tt/. (Accessed on 14 November 2025).

Clerbaux, C., Boynard, A., Clarisse, L., George, M., Hadji-Lazaro, J., Herbin, H., Hurtmans, D., Pommier, M., Razavi, A., Turquety, S., Wespes, C., Coheur, P.F., 2009. Monitoring of atmospheric composition using the thermal infrared IASI/MetOp sounder. Atmos. Chem. Phys. 9, 6041–6054. http://dx.doi.org/10.5194/acp-9-6041-2009.

Cogliati, S., Sarti, F., Chiarantini, L., Cosi, M., Lorusso, R., Lopinto, E., Miglietta, F., Genesio, L., Guanter, L., Damm, A., Pérez-López, S., Scheffler, D., Tagliabue, G., Panigada, C., Rascher, U., Dowling, T., Giardino, C., Colombo, R., 2021. The PRISMA imaging spectroscopy mission: overview and first performance analysis. Remote Sens. Environ. 262, 112499. http://dx.doi.org/10.1016/j.rse.2021.112499.

Cusworth, D., Duren, R., Thorpe, A., Pandey, S., Maasakkers, J., Aben, I., Jervis, D., Varon, D., Jacob, D., Randles, C., Gautam, R., Omara, M., Schade, G., Dennison, P., Frankenberg, C., Gordon, D., Lopinto, E., Miller, C., 2021. Multisatellite imaging of a gas well blowout enables quantification of total methane emissions. Geophys. Res. Lett. (48), http://dx.doi.org/10.1029/2020GL090864.

Cusworth, D.H., Jacob, D.J., Sheng, J.-X., Benmergui, J., Turner, A.J., Brandman, J., White, L., Randles, C.A., 2018. Detecting high-emitting methane sources in oil/gas fields using satellite observations. Atmospheric Chem. Phys. 18 (23), 16885–16896, URL https://acp.copernicus.org/articles/18/16885/2018/.

Cusworth, D.H., Jacob, D.J., Varon, D.J., Chan Miller, C., Liu, X., Chance, K., Thorpe, A.K., Duren, R.M., Miller, C.E., Thompson, D.R., Frankenberg, C., Guanter, L., Randles, C.A., 2019. Potential of next-generation imaging spectrometers to detect and quantify methane point sources from space. Atmospheric Meas. Tech. 12 (10), 5655–5668, URL https://amt.copernicus.org/articles/12/5655/2019/.

Deonar, 2025. https://indianexpress.com/article/cities/mumbai/at-deonar-dumping-site-toxicology-indicators-four-times-safety-limit-study-10054186/. (Accessed on 14 November 2025).

ERA5, https://www.ecmwf.int/en/forecasts/dataset/ecmwf-reanalysis-v5. (Accessed: 9 January 2025).

Etiope, G., Ciotoli, G., Schwietzke, S., Schoell, M., 2019. Gridded maps of geological methane emissions and their isotopic signature. Earth Syst. Sci. Data 11, 1–22. http://dx.doi.org/10.5194/essd-11-1-2019, 2019.

Foote, M.D., Dennison, P.E., Sullivan, P.R., O'Neill, K.B., Thorpe, A.K., Thompson, D.R., Cusworth, D.H., Duren, R., Joshi, S.C., 2021. Impact of scene-specific enhancement spectra on matched filter greenhouse gas retrievals from imaging spectroscopy. Remote Sens. Environ. (ISSN: 0034-4257) 264 (2021), 112574. http://dx.doi.org/10.1016/j.rse.2021.112574.

Foote, M.D., Dennison, P.E., Thorpe, A.K., Thompson, D.R., Jongaramrungruang, S., Frankenberg, C., Joshi, S.C., 2020. Fast and accurate retrieval of methane concentration from imaging spectrometer data using sparsity prior. IEEE Trans. Geosci. Remote Sens. 58 (9), 6480–6492.

Frankenberg, C., Thorpe, A.K., Thompson, D.R., Hulley, G., Kort, E.A., Vance, N., Borchardt, J., Krings, T., Gerilowski, K., Sweeney, C., Conley, S., Bue, B.D., Aubrey, A.D., Hook, S., Green, R.O., 2016. Airborne methane remote measurements reveal heavy-tail flux distribution in four corners region. Proc. Natl. Acad. Sci. 113 (35), 9734–9739.

Fratticioli, C., Trisolino, P., Maione, M., Calzolari, C., Biron, D., Amendola, S., Steinbacher, M., Cristofanelli, P., 2023. Continuous atmospheric in-situ measurements of the CH4/CO ratio at the Mt. Cimone station (Italy, 2165 m a.s.l.) and their possible use for estimating regional CH4 emissions. Environ. Res. (ISSN: 0013-9351) 232, 116343. http://dx.doi.org/10.1016/j.envres.2023.116343, 2023.

GCP, 2023. https://www.globalcarbonproject.org/. (Accessed: 20 February 2023).

Graven, H., Keeling, R.F., Rogelj, J., 2020. Changes to carbon isotopes in atmospheric CO2 over the industrial era and into the future. Glob. Biogeochem. Cycles 34, e2019GB006170. http://dx.doi.org/10.1029/2019GB006170.

Guanter, L., Irakulis-Loitxate, I., Gorroño, J., Sánchez-García, E., Cusworth, D.H., Varon, D.J., Cogliati, S., Colombo, R., 2021. Mapping methane point emissions with the PRISMA spaceborne imaging spectrometer. Remote Sens. Environ. (ISSN: 0034-4257) 265, http://dx.doi.org/10.1016/j.rse.2021.112671, URL: https://www.sciencedirect.com/science/article/pii/S0034425721003916.

Han, Y., Revercomb, H., Cromp, M., Gu, D., Johnson, D., Mooney, D., Scott, D., Strow, L., Bingham, G., Borg, L., Chen, Y., DeSlover, D., Esplin, M., Hagan, D., Jin, X., Knuteson, R., Motteler, H., Predina, J., Suwinski, L., Zavyalov, V., 2013. Suomi NPP CrIS measurements, sensor data record algorithm, calibration and validation activities, and record data quality. J. Geophys. Res.: Atmospheres 118. http://dx.doi.org/10.1002/2013JD020344.

IMEO, 2025. https://www.unep.org/topics/energy/methane/international-methane-emissions-observatory. (Accessed on 14 November 2025).

IPCC, 2023. Climate change 2023: Synthesis report. In: Core Writing Team, Lee, H., Romero, J. (Eds.), Contribution of Working Groups I, II and III To the Sixth Assessment Report of the Intergovernmental Panel on Climate Change. IPCC, Geneva, Switzerland, pp. 35–115. http://dx.doi.org/10.59327/IPCC/AR6-9789291691647.

Jervis, D., McKeever, J., Durak, B.O.A., Sloan, J.J., Gains, D., Varon, D.J., Ramier, A., Strupler, M., Tarrant, E., 2021. The ghgsat-d imaging spectrometer. Atmospheric Meas. Tech. 14 (3), 2127–2140, URL https://amt.copernicus.org/articles/14/2127/2021/.

Kambhatla, N., Leen, T.K., 1994. Classifying with Gaussian mixtures and clustering. In: Advancements in Neural Information Processing Systems, vol. 7, (NIPS 1994).

Kanjurmarg, 2025. https://www.freepressjournal.in/mumbai/mumbai-news-kanjurmarg-mulund-residents-seek-shrc-intervention-over-toxic-air-from-dumping-ground-pollution. (Accessed on 14 November 2025).

Korkin, S., Sayer, A.M., Ibrahim, A., Lyapustin, A., 2022. A practical guide to writing a radiative transfer code. Comput. Phys. Comm. (ISSN: 0010-4655) 271, http://dx.doi.org/10.1016/j.cpc.2021.108198, URL https://www.sciencedirect.com/science/article/pii/S0010465521003106.

Kurtén, T., Zhou, L., Makkonen, R., Merikanto, J., Räisänen, P., Boy, M., Richards, N., Rap, A., Smolander, S., Sogachev, A., Guenther, A., Mann, G.W., Carslaw, K., Kulmala, M., 2011. Large methane releases lead to strong aerosol forcing and reduced cloudiness. Atmos. Chem. Phys. 11, 6961–6969. http://dx.doi.org/10.5194/acp-11-6961-2011.

Kuze, A., Suto, H., Nakajima, M., Hamazaki, T., 2009. Thermal and near infrared sensor for carbon observation Fourier-transform spectrometer on the greenhouse gases observing satellite for greenhouse gases monitoring. Appl. Opt. 48, 6716–6733.

Laughner, J.L., Neu, J.L., Schimel, D., Wennberg, P.O., Barsanti, K., Bowman, K.W., Chatterjee, A., Croes, B.E., Fitzmaurice, H.L., Henze, D.K., Kim, J., Kort, E.A., Liu, Z., Miyazaki, K., Turner, A.J., Anenberg, S., Avise, J., Cao, H., Crisp, D., et al., 2021. Societal shifts due to COVID-19 reveal large-scale complexities and feedbacks between atmospheric chemistry and climate change. Proc. Natl. Acad. Sci. USA 118 (46), e2109481118. http://dx.doi.org/10.1073/pnas.2109481118.

lblRTM, 2023. http://rtweb.aer.com/lblrtm.html. (Accessed: 20 February 2023).

Li, K., Bai, K., Fu, P., Jiao, P., Chen, H., Huang, X., Liu, C., Chang, N.-B., 2025. SSRMF: A sparse spectral reconstruction enhanced matched filter for improving point-source methane emission detection in complex terrain. ISPRS J. Photogramm. Remote Sens. 225 (0924), 238-256-2716. http://dx.doi.org/10.1016/j.isprsjprs.2025.04.034.

Michel, S.E., Lan, X., Miller, J., Tans, P., Clark, J.R., Schaefer, H., Sperlich, P., Brailsford, G., Morimoto, S., Moossen, H., Li, J., 2024. Rapid shift in methane carbon isotopes suggests microbial emissions drove record high atmospheric methane growth in 2020–2022. Proc. Natl. Acad. Sci. USA 121 (44), e2411212121. http://dx.doi.org/10.1073/pnas.2411212121.

Mulund, 2025. https://www.freepressjournal.in/mumbai/mumbai-mulund-dumping-ground-closure-faces-delay-bmc-sets-target-to-process-15000-tonnes-of-waste-daily-by-june-2025. (Accessed on 14 November 2025).

Myhre, G., Shindell, D., Breon, F.M., Collins, W., Fuglestvedt, J., 2013. Anthropogenic and natural radiative forcing supplementary information. In: Climate Change 2013: The Physical Science Basis.

Nisbet, E.G., Dlugokencky, E.J., Manning, M.R., Lowry, D., Fisher, R.E., France, J.L., Michel, S.E., Miller, J.B., White, J.W.C., Vaughn, B., Bousquet, P., Pyle, J.A., Warwick, N.J., Cain, M., Brownlow, N., Zazzeri, G., Lanoisellé, M., Manning, A.C., Gloor, E., Worthy, D.E.J., Brunke, E.G., Labuschagne, C., Wolff, E.W., Ganesan, A.L., 2016. Rising atmospheric methane: 2007–2014 growth and isotopic shift. Glob. Biogeochem. Cycles 30, 1356–1370. http://dx.doi.org/10.1002/2016GB005406.

Omidi, A., Bourlon, E., Khaleghi, A., Tarakki, N., Martino, R., Stuart, J., Risk, D., 2025. Most landfill methane emissions escape detection in EPA21 surface emission monitoring surveys. Waste Manage. (ISSN: 0956-053X) 207, 115104. http://dx.doi.org/10.1016/j.wasman.2025.115104.

Pandey, S., Gautam, R., Houweling, S., van der Gon, H.D., Sadavarte, P., Borsdorff, T., Hasekamp, O., Landgraf, J., Tol, P., van Kempen, T., Hoogeveen, R., van Hees, R., Hamburg, S.P., Maasakkers, J.D., Aben, I., 2019. Satellite observations reveal extreme methane leakage from a natural gas well blowout. Proc. Natl. Acad. Sci. 116 (52), 26376–26381.

Pei, Z., Han, G., Mao, H., Chen, C., Shi, T., Yang, K., Ma, X., Gong, W., 2023. Improving quantification of methane point source emissions from imaging spectroscopy. Remote Sens. Environ. (ISSN: 0034-4257) 295, 113652. http://dx.doi.org/10.1016/j.rse.2023.113652, 2023.

Peng, S., Lin, X., Thompson, R.L., et al., 2022. Wetland emission and atmospheric sink changes explain methane growth in 2020. Nature 612, 477–482. http://dx.doi.org/10.1038/s41586-022-05447-w.

Remedios, J.J., Leigh, R.J., Waterfall, A.M., Moore, D.P., Sembhi, H., Parkes, I., Greenhough, J., Chipperfield, M.P., Hauglustaine, D., 2007. MIPAS reference atmospheres and comparisons to V4.61/V4.62 MIPAS level 2 geophysical data sets. Atmos. Chem. Phys. Discuss. 7, 9973–10017. http://dx.doi.org/10.5194/acpd-7-9973-2007.

Sand, M., Skeie, R.B., Sandstad, M., et al., 2023. A multi-model assessment of the global warming potential of hydrogen. Commun Earth Env. 4, 203. http://dx.doi.org/10.1038/s43247-023-00857-8.

Saunois, M., Martinez, A., Poulter, B., Zhang, Z., Raymond, P.A., Regnier, P., Canadell, J.G., Jackson, R.B., Patra, P.K., Bousquet, P., Ciais, P., Dlugokencky, E.J., Lan, X., Allen, G.H., Bastviken, D., Beerling, D.J., Belikov, D.A., Blake, D.R., Castaldi, S., Crippa, M., Deemer, B.R., Dennison, F., Etiope, G., Gedney, N., Höglund-Isaksson, L., Holgerson, M.A., Hopcroft, P.O., Hugelius, G., Ito, A., Jain, A.K., Janardanan, R., Johnson, M.S., Kleinen, T., Krummel, P.B., Lauerwald, R., Li, T., Liu, X., McDonald, K.C., Melton, J.R., Mühle, J., Müller, J., Murguia-Flores, F., Niwa, Y., Noce, S., Pan, S., Parker, R.J., Peng, C., Ramonet, M., Riley, W.J., Rocher-Ros, G., Rosentreter, J.A., Sasakawa, M., Segers, A., Smith, S.J., Stanley, E.H., Thanwerdas, J., Tian, H., Tsuruta, A., Tubiello, F.N., Weber, T.S., van der Werf, G.R., Worthy, D.E.J., Xi, Y., Yoshida, Y., Zhang, W., Zheng, B., Zhu, Q., Zhu, Q., Zhuang, Q., 2025. Global methane budget (2025) 2000–2020. Earth Syst. Sci. Data 17, 1873–1958. http://dx.doi.org/10.5194/essd-17-1873-2025.

Schaum, A., 2021. A uniformly most powerful of gas plumes against a cluttered background. Remote Sens. Environ. 260, 112443. http://dx.doi.org/10.1016/j.rse.2021.112443.

Smith, N., Weisz, E., Huang, H.-L., Annegarn, H.J., 2007. Retrieval of total column methane concentration from IR sounding measurements. In: IEEE International Geoscience and Remote Sensing Symposium. Barcelona, Spain, pp. 4398–4400. http://dx.doi.org/10.1109/IGARSS.2007.4423828.

Suto, H., Kataoka, F., Kikuchi, N., Knuteson, R.O., Butz, A., Haun, M., Buijs, H., Shiomi, K., Imai, H., Kuze, A., 2021. Thermal and near-infrared sensor for carbon observation Fourier transform spectrometer-2 (TANSO-FTS-2) on the Greenhouse gases observing satellite-2 (GOSAT-2) during its first year in orbit. Atmos. Meas. Tech. 14, 2013–2039. http://dx.doi.org/10.5194/amt-14-2013-2021.

Thompson, D.R., Thorpe, A.K., Frankenberg, C., Green, R.O., Duren, R., Guanter, L., Hollstein, A., Middleton, E., Ong, L., Ungar, S., 2016. Space-based remote imaging spectroscopy of the aliso canyon ch4 superemitter. Geophys. Res. Lett. 43 (12), 6571–6578. http://dx.doi.org/10.1002/2016GL069079, URL https://agupubs.onlinelibrary.wiley.com/.

Thorpe, A.K., Frankenberg, C., Roberts, D.A., 2014. Retrieval techniques for airborne imaging of methane concentrations using high spatial and moderate spectral resolution: application to aviris. Atmospheric Meas. Tech. 7 (2), 491–506, URL https://amt.copernicus.org/articles/7/491/2014/.

Thorpe, A.K., Frankenberg, C., Thompson, D.R., Duren, R.M., Aubrey, A.D., Bue, B.D., Green, R.O., Gerilowski, K., Krings, T., Borchardt, J., Kort, E.A., Sweeney, C., Conley, S., Roberts, D.A., Dennison, P.E., 2017. Airborne doas retrievals of methane, carbon dioxide, and water vapor concentrations at high spatial resolution: application to aviris-ng. Atmospheric Meas. Tech. 10 (10), 3833–3850, URL https://amt.copernicus.org/articles/10/3833/2017/.

United Nations Environment Programme, 2021. Global methane assessment: benefits and costs of mitigating methane emissions. https://www.unep.org/resources/report/global-methane-assessment-benefits-and-costs-mitigating-methane-emissions.

Varon, D.J., Jacob, D.J., Jervis, D., McKeever, J., 2020a. Quantifying time-averaged methane emissions from individual coal mine vents with GHGSat-D satellite observations. Environ. Sci. Technol. 54 (16), 10246–10253. http://dx.doi.org/10.1021/acs.est.0c01213, pMID: 32672947.

Varon, D.J., Jacob, D.J., McKeever, J., Jervis, D., Durak, B.O.A., Xia, Y., Huang, Y., 2018. Quantifying methane point sources from fine-scale satellite observations of atmospheric methane plumes. Atmospheric Meas. Tech. 11 (10), 5673–5686, URL https://amt.copernicus.org/articles/11/5673/2018/.

Varon, D.J., Jervis, D., McKeever, J., Spence, I., Gains, D., Jacob, D.J., 2020b. High-frequency monitoring of anomalous methane point sources with multispectral sentinel-2 satellite observations. Atmospheric Meas. Tech. Discuss. 2020, 1–21, URL https://amt.copernicus.org/preprints/amt-2020-477/.

Varon, D.J., McKeever, J., Jervis, D., Maasakkers, J.D., Pandey, S., Houweling, S., Aben, I., Scarpelli, T., Jacob, D.J., 2019. Satellite discovery of anomalously large methane point sources from oil/gas production. Geophys. Res. Lett. 46 (22), 13507–13516. http://dx.doi.org/10.1029/2019GL083798, URL https://agupubs.onlinelibrary.wiley.com/.

Veefkind, J., Aben, I., McMullan, K., Förster, H., de Vries, J., Otter, G., Claas, J., Eskes, H., de Haan, J., Kleipool, Q., van Weele, M., Hasekamp, O., Hoogeveen, R., Landgraf, J., Snel, R., Tol, P., Ingmann, P., Voors, R., Kruizinga, B., Vink, R., Visser, H., Levelt, P., 2012. Tropomi on the esa sentinel-5 precursor: A gmes mission for global observations of the atmospheric composition for climate, air quality and ozone layer applications. Remote Sens. Environ. 120, 70–83, the Sentinel Missions - New Opportunities for Science. URL https://www.sciencedirect.com/science/article/pii/S0034425712000661.

Vieth, A., Wilkes, H., 2010. Stable isotopes in understanding origin and degradation processes of petroleum. http://dx.doi.org/10.1007/978-3-540-77587-4_5.

Zazzeri, G., Lowry, D., Fisher, R.E., France, J.L., Lanoisellé, M., Kelly, B.F.J., Necki, J.M., Iverach, C.P., Ginty, E., Zimnoch, M., Jasek, A., Nisbet, E.G., 2016. Carbon isotopic signature of coal-derived methane emissions to the atmosphere: from coalification to alteration. Atmos. Chem. Phys. 16, 13669–13680. http://dx.doi.org/10.5194/acp-16-13669-2016.

Zazzeri, G., Lowry, D., Fisher, R.E., France, J.L., Lanoisellé, M., Nisbet, E.G., 2015. Plume mapping and isotopic characterisation of anthropogenic methane sources. Atmos. Environ. (ISSN: 1352-2310) 110 (2015), 151–162. http://dx.doi.org/10.1016/j.atmosenv.2015.03.029.

Zazzeri, G., Lowry, D., Fisher, R.E., et al., 2017. Evaluating methane inventories by isotopic analysis in the London region. Sci. Rep. 7 (2017), 4854. http://dx.doi.org/10.1038/s41598-017-04802-6.

Zhang, Y., Gautam, R., Pandey, S., Omara, M., Maasakkers, J.D., Sadavarte, P., Lyon, D., Nesser, H., Sulprizio, M.P., Varon, D.J., Zhang, R., Houweling, S., Zavala-Araiza, D., Alvarez, R.A., Lorente, A., Hamburg, S.P., Aben, I., Jacob, D.J., 2020. Quantifying methane emissions from the largest oil-producing basin in the united states from space. Sci. Adv. 6 (17), URL https://advances.sciencemag.org/content/6/17/eaaz5120.